



Norwegian University of  
Science and Technology

---

# Hyperspectral Imager Calibration and Characterisation

---

Marie Bøe Henriksen

Department of  
Engineering Cybernetics

Supervisor: Tor Arne Johansen

Co-supervisor: Fred Sigernes

18th December 2018



## Abstract

Algal blooms and other oceanographic phenomena will be detected by hyperspectral imagers from air- and spaceborne platforms among others, as a part of the Hyperspectral Smallsat for Ocean Observation (HYPSO) mission. For the collected data to be usable, the hyperspectral instruments must be calibrated and characterised before use. The goal of this project is therefore to set up calibration procedures for spectral and radiometric calibration of hyperspectral imagers (HSIs), and test these procedures by calibrating several imagers. Spectral calibration was set up and performed on two imagers, the HSI V4C and HSI V6, and the results compared. Radiometric calibration was divided into two parts, finding the dark current and measuring radiance from a known standard light source. These parts were performed on different imagers, so no full calibration was completed, but results from the different parts are presented. After calibration, there may still be unwanted effects in the system distorting the data. These effects should be characterised to minimise errors. The second goal of this project is therefore to detect and correct for some of these effects. This project focuses on the effects from spectral and spatial misregistrations in the system, called smile and keystone, respectively. Smile was detected using data from the spectral calibration, and corrections were made. The spectral bandpass was also estimated. A challenge when detecting keystone in an imager used for remote sensing is to have the targeted pattern in focus. To obtain infinity focus on short distances, a collimator set-up was therefore designed and built. This set-up was tested with a normal camera, but keystone detection on hyperspectral data will be a part of future work.



### **Acknowledgements**

I would like to thank Fred Sigernes for his help on designing the collimator set-up used in this project, and Lise Lyngsnes Randeberg for letting us use the optical calibration lab at NTNU. I would also like to thank the NTNU SmallSat team, and especially Elizabeth Prentice for collaboration on the calibration procedures and data collection, and Joe Garrett for making the scripts used for spectral calibration and smile correction.



# Table of Contents

Abstract	i
Acknowledgements	ii
Table of Contents	iii
List of Abbreviations	v
<b>1 Introduction</b>	<b>1</b>
<b>2 Background Theory</b>	<b>5</b>
2.1 Hyperspectral Imaging . . . . .	5
2.1.1 Definitions . . . . .	6
2.1.2 Imaging System . . . . .	8
2.1.3 Remote Sensing . . . . .	14
2.2 Calibration . . . . .	15
2.2.1 Spectral Calibration . . . . .	16
2.2.2 Radiometric Calibration . . . . .	16
2.3 Characterisation . . . . .	18
2.3.1 Spectral and Spatial Misregistrations . . . . .	18
2.3.2 Detection Methods . . . . .	20
2.3.3 Correction Methods . . . . .	21
<b>3 Methods</b>	<b>23</b>
3.1 Equipment . . . . .	23
3.1.1 HSI V4C and HSI V6 . . . . .	25
3.1.2 Collimator Set-up . . . . .	26
3.2 Spectral Calibration . . . . .	28
3.3 Radiometric Calibration . . . . .	30
3.4 Characterisation . . . . .	31

3.4.1	Spectral Misregistrations (Smile) . . . . .	31
3.4.2	Spectral Bandpass . . . . .	32
3.4.3	Spatial Misregistrations (Keystone) . . . . .	32
<b>4</b>	<b>Results and Discussion</b>	<b>33</b>
4.1	Spectral Calibration . . . . .	33
4.2	Radiometric Calibration . . . . .	36
4.3	Characterisation . . . . .	40
4.3.1	Spectral Misregistrations (Smile) . . . . .	40
4.3.2	Spectral bandpass . . . . .	42
<b>5</b>	<b>Conclusion and Further Work</b>	<b>45</b>
	<b>References</b>	<b>47</b>
	<b>Appendices</b>	<b>51</b>
<b>A</b>	<b>Lamp Certificate, ISS-30-VA</b>	<b>53</b>

# List of Abbreviations

AMOS	Center for Autonomous Marine Operations and Systems
AoI	Area of interest
ASV	Autonomous surface vehicle
AUV	Autonomous underwater vehicle
CHB	Calibration Home Base
CubeSat	U-class spacecraft
DLR	German Aerospace Center
DN	Digital number
EnMAP	Environmental Mapping and Analysis Program
EO	Earth observation
EXP	Exposure time
FFI	Norwegian Defence Research Establishment
FOV	Field of view
FPA	Focal plane array
FPS	Frames per second
FWHM	Full width at half maximum
GCP	Geometric control point calibration
HICO	Hyperspectral Imager for the Coastal Ocean
HSI	Hyperspectral imager
HYPSO	Hyperspectral Smallsat for Ocean Observation
HypIRI	Hyperspectral Infrared Imager
IDS	Imaging Development Systems
NIST	National Institute of Standards and Technology
NTNU	Norwegian University of Science and Technology
PSF	Point spread function

SNR	Signal-to-noise ratio
SmallSat	Small satellite
TMC	Technical Manufacturing Corporation
UAV	Unmanned aerial vehicle
UNIS	University Centre in Svalbard
UV	Ultraviolet
VNIR	Visible and near-infrared

# 1 | Introduction

Hyperspectral imaging, also known as imaging spectroscopy, is an imaging technique used to combine two dimensional spatial data with a third dimension of spectral data. The data collected is therefore often called a "hyperspectral data cube", or simply a "hyperspectral cube". In this report, two hyperspectral imagers (HSIs) are calibrated and characterised to ensure better quality of the data obtained. For a hyperspectral instrument, spectral information from hundreds of narrow bands can be obtained. This is done by recording radiance in, and near, the visible spectrum. A similar instrument is the multispectral imager, which is based on the same technology, but records information from fewer, and often wider, spectral bands. A more detailed explanation of the hyperspectral imager and how it works is given in Section 2.1.

In the early development of hyperspectral imaging systems, the instruments were mainly oriented towards remote sensing applications [1]. Data acquired from these types of operations can be used within disciplines such as oceanography, precision farming, forestry and geology, among others [2]. For oceanographic purposes, detection and classification of algae is one possible application. Algal blooms can produce vividly coloured displays from the algae cells accumulating on the water surface. The blooms can be friendly, but some may also be harmful due to their production of internal toxins, their sheer biomass, or their physical shape, as mentioned in [3]. The toxins produced may kill fish and shellfish, and also harm human consumers. Death of birds and mammals related to harmful algal blooms and their toxins have also been recorded, giving huge public and economic concerns when they occur. High biomass accumulation of algae can lead to environmental damage, including hypoxia, anoxia, and shading of submerged vegetation. This may further lead to a multitude of negative environmental consequences. As mentioned in [4], cases of animals being poisoned by drinking water containing toxins from algal blooms in freshwater systems have also been reported. Even though less than 2% of some 5000 species of marine microalgae described worldwide are known to be harmful or toxic, the percentage appears to be increasing.

Events such as algal blooms are easily detected using optical instruments, due to the blooms' clear surface signatures in the optical domain. Information acquired using a hyperspectral imager can be used to detect algal blooms as they appear, identify them and characterise

their spatial extent, as well as observe other phenomena happening in the visible and near-infrared (VNIR) spectrum [5]. This is the background motivation for the Hyperspectral Smallsat for Ocean Observation (HYPSO) mission [6], which is a satellite mission initiated by the Norwegian University of Science and Technology (NTNU) Small Satellite (SmallSat) Lab. The SmallSat Lab focuses on designing, building and operating small satellites for observing the Norwegian coastline and its oceanographic domain. As described in [5], the HYPSO satellite will observe the ocean along the Norwegian coast, specifically targeted to detect algal blooms, phytoplankton, river plumes, and so on. A slew manoeuvre will be performed to increase the effective spatial resolution and the signal-to-noise ratio (SNR) by obtaining several overlapping images from the targeted area. The use of hyperspectral sensors in a spaceborne mission is no new idea, however. Other earth observation (EO) missions such as EO-1, with the instrument Hyperion [7], and Hyperspectral Imager for the Coastal Ocean (HICO) mission [8], among others, have previously used HSIs for collecting data. There are also other missions planned for the near future, such as Environmental Mapping and Analysis Program (EnMAP), and Hyperspectral Infrared Imager (HyspIRI), as mentioned in [9]. These satellites are all larger satellites, which makes them a lot more expensive. The HYPSO satellite, on the other hand, is a U-class spacecraft (CubeSat), which is much smaller and costs less both to produce and to launch. This gives an opportunity to produce more satellites and make them work together to increase temporal coverage and redundancy.

The HYPSO mission is a project under the Center for Autonomous Marine Operations and Systems (AMOS). After launch, the satellite will work together with autonomous underwater vehicles (AUVs), autonomous surface vehicles (ASVs) and unmanned aerial vehicles (UAVs). They will execute coordinated missions to obtain more information from the area of interest, creating an autonomous multi-agent system for marine observations [5]. Hyperspectral data from the satellite can, for example, be used to detect a potential harmful algal bloom. UAVs, also equipped with an HSI, can be sent off to investigate the algal bloom further, giving a better resolution view of a smaller part of the targeted area. ASVs can be used to collect in-situ measurements, such as water samples to investigate the algae further in the lab, and AUVs can be deployed to collect information from underneath the water surface, since the air- and spaceborne instruments only collect information from the upper layers of the ocean.

Space- and airborne instruments require proper characterisation before use, as possibilities for performing characterisation procedures after launch are very limited. If the instrument is not calibrated and characterised well enough, the data provided by the sensor will in

worst case be deemed unusable for the planned applications [2]. Characterisation refers in this report to the act of describing distinctive characteristics of the imager, while calibration is the act of setting parameters of the imager by comparing the performance with known standards. For a hyperspectral imager, calibration is needed to provide necessary information about the recorded data. Spectral calibration gives the relationship between the pixel number and corresponding wavelength value, while the radiometric calibration provides the relationship between sensor count and true radiance. Characterisation of the sensor is also needed to make corrections for effects corrupting the data, and to determine uncertainties inherent in the measurements.

Some of these unwanted effects in hyperspectral imagers are from spectral and spatial misregistrations, commonly referred to as smile and keystone. These are the main effects in focus in this report, and are described further in Section 2.3.1. Other effects that should be characterised includes linearity of the sensor's response, dynamic range, temperature dependence, stray light, and polarisation sensitivity, as mentioned in [10]. Characterising these effects will be a part of future work of this project.

There are several places in the world that have the equipment and knowledge on how to calibrate and characterise a hyperspectral imager. Some examples are the Calibration Home Base (CHB) at the German Aerospace Center (DLR) in Germany[11], and the optical lab at Norwegian Defence Research Establishment (FFI). There is also a lab for radiometric calibration at the University Centre in Svalbard (UNIS). Sending the imager to different locations costs time and money, and there is no guarantee that the imager is still fully calibrated after transportation back from the calibration lab. Vibrations and other external factors may affect the imager, which can result in minor physical changes in the system and give the need for a new calibration. That the calibration may be invalid after transportation is also the reason why the imager must be re-calibrated after launch, when being used for remote sensing [12].

A radiometric sphere and four spectral lamps, further described in Section 3.1, are available for radiometric and spectral calibration at NTNU. Time is a critical factor in the HYPSON mission, as NTNU SmallSat Lab intends to have a continuous pipeline of spacecraft in an ongoing process of development, test and operations [6]. The ability to calibrate the hyperspectral imager at NTNU is therefore highly beneficial for NTNU SmallSat Lab in terms of the HYPSON mission and future hyperspectral missions.

This project therefore aims to set up spectral and radiometric calibration procedures and perform these on hyperspectral imagers using the existing equipment at NTNU, and further investigate a method for detecting smile and keystone effects in such imagers.

The remainder of this report is divided into four chapters. Chapter 2 gives some background information regarding optics theory and hyperspectral imaging, it also includes calibration theory and some previous work on characterisation procedures. In Chapter 3 the equipment used is described, as well as the calibration and characterisation set-ups and procedures used in this project. The results are presented and discussed in Chapter 4, and Chapter 5 holds the conclusion and outlines further work that describes what can be done to improve the calibration procedures and expand the characterisation process.

## 2 | Background Theory

This chapter introduces some background theory relevant to this project. Section 2.1 starts off by defining optical terms, explaining general imaging systems and introducing the concept of hyperspectral imaging. Section 2.2 continues by presenting the spectral and radiometric calibrations. Finally, misregistration errors and what can and have been done to characterise and correct for such effects are described in the Section 2.3.

### 2.1 Hyperspectral Imaging

Hyperspectral imaging, also known as imaging spectroscopy, is an imaging technique to capture information from several spectral bands from the same spatial area at approximately the same time. There are several ways of building a hyperspectral imager. Among these are using a prism, grating or a combination of both in the optical design, and use the pushbroom or whiskbroom technique to obtain a full spatial image. Another option is to use a snapshot imager that captures the full hyperspectral cube at once using a sensor with many layers to obtain information from the different wavelengths at the same time as capturing 2D spatial information. Other methods include using filters, as done in [13], or filter wheels. One filter for each bands becomes impractical quite fast, however, when moving from multispectral imaging with only a few spectral bands, to hyperspectral imaging with potentially hundreds of bands.

The quality of the final images depends primarily on the imaging optics, the detector and associated electronics, and the processing of the raw data. To achieve high quality images, it is important to understand how the imaging optics transfers radiance from an object to the image plane, and why this is the goal of the system.

This section starts off introducing some relevant terminology and units used when observing radiation, like light. Further, theory for understanding imaging systems in general is presented, and elements typically used in hyperspectral designs is introduced. The hyperspectral imagers used in this project are based on the pushbroom design, so the theory presented in this section focuses on this type of imagers. This section is mainly based on the theory found in [1], [14] and [15].

### 2.1.1 Definitions

This section introduces some of the terminology, as well as some of the important units, used later both within this chapter and throughout the report.

#### Solid angle

The solid angle,  $\Omega$  is defined as

$$\Omega = \frac{A}{r^2},$$

where  $A$  is the area of a sphere segment, and  $r$  the radius of the sphere. The solid angle is measured in steradians, or square radians,  $[sr]$ . An illustration can be seen in Figure 2.1.

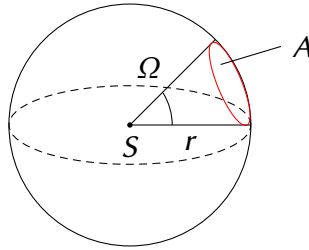


Figure 2.1: Definition of solid angle,  $\Omega$ , where  $S$  is the source point,  $r$  the radius of the sphere, and  $A$  the area of a sphere segment.

#### Flux, intensity and radiance

The *radiant flux*,  $\Phi_e$ , in the system is defined as the number of the radiant energy emitted from a source,  $S$ , per unit time into a solid angle,  $\Omega$ , so that

$$[\Phi_e] = W.$$

*Intensity*,  $I$ , is further defined as the radiant flux per unit solid angle,

$$[I] = \frac{W}{sr}.$$

*Radiance*,  $B$ , is then defined as the intensity through a unit surface area, or radiant flux per unit projected area and solid angle,

$$[B] = \frac{W}{m^2 sr},$$

and *irradiance*,  $E$ , is defined as the power incident on or passing through a unit surface area,

$$[E] = \frac{W}{m^2}.$$

Further, *spectral radiance*,  $B_\lambda$ , and *spectral irradiance*,  $E_\lambda$ , are defined as radiance per wavelength and irradiance per wavelength, respectively,

$$[B_\lambda] = \frac{W}{m^2 m sr} \quad \text{and} \quad [E_\lambda] = \frac{W}{m^2 m}.$$

### Reflectance, transmittance and absorptance

The term *reflectance* describes the fraction of light that is reflected from a surface. A *reflectance spectrum* is a plot of reflectance as a function of wavelength. *Transmittance* describes the fraction of light that passes through a substance. The transmittance of an object can be described by its *transmission coefficient*. Further, *absorptance* is a measure of the rate of decrease in the light intensity as it passes through a substance. This should not be confused with *absorbance*, which refers to the physical process of absorbing light.

### Interference and diffraction

*Interference* is the result of individual wave sources interacting with each other, while *diffraction* is caused by a wave distorted by an obstacle. An illustration of interference and diffraction can be seen in Figure 2.2.

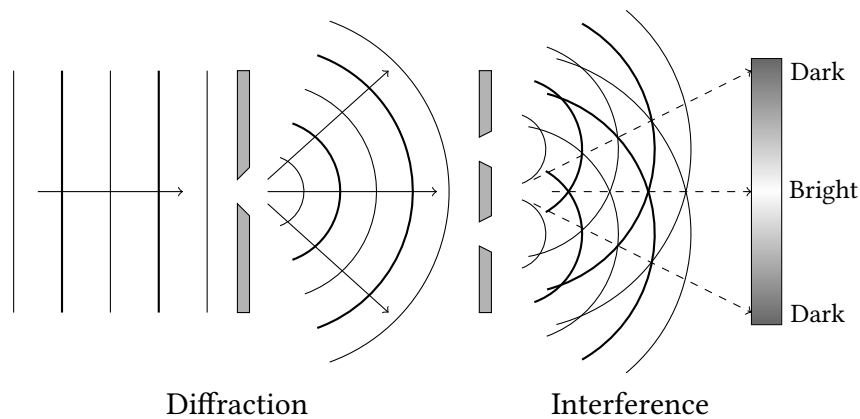


Figure 2.2: Illustration of diffraction as the light is distorted by an obstacle, and interference as two wave sources interact with each other resulting in an interference pattern.

### 2.1.2 Imaging System

In an imaging system, the *optical axis* is the straight line that passes through the centres of curvature of the lenses in the system, as seen in Figure 2.3.

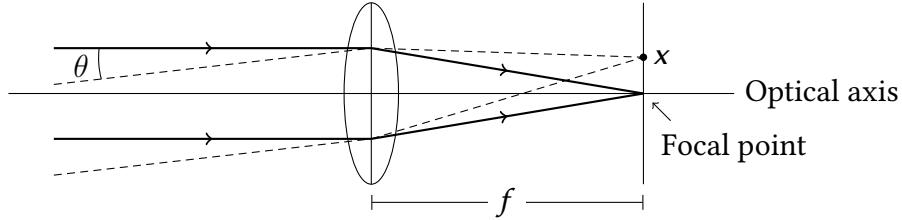


Figure 2.3: Illustration of the optical axis, and the focal length  $f$ .  $\theta$  denotes the angle of the incident wave, and  $x$  the shift in the image plane. Based on illustration from [15].

Rays that are close or parallel to the optical axis, also known as *paraxial rays*, converge at a point on the axis called the *focal point*. Extending this point into a plane perpendicular to the optical axis gives the *focal plane*, which is where the image is focused. The scale of the image is further defined by the *focal length*,  $f$ , which is the distance between the centre of the front lens and the focal point. If  $x$  is the shift in image point in the focal plane for a tilt,  $\theta$ , in the incident wave on the lens, the focal length is given by

$$f = \frac{x}{\tan \theta}.$$

The *f-number*,  $F/\#$ , is further defined as

$$F/\# = \frac{f}{D},$$

where  $f$  is the focal length and  $D$  is the aperture of the system. A higher f-number will give a smaller opening for the light to pass through, so that only the light from a smaller area reaches the sensor, and will therefore result in less light on the sensor.

The *field of view* (FOV) of the imager is defined as the angle where incoming light is detected. FOV is given by the aperture, which limits the extent of the scene imaged. In Earth imaging cameras, it is usually the detector that limits the FOV of the imaging system.

## Grating

A key optical element in the design of a pushbroom hyperspectral imager is the grating. There are several types of gratings, and they can also be used in combination with prisms. A *diffraction grating* consists of a number,  $N$ , of single slits, with the width  $b$  of each slit, placed with an equal spacing  $a$ . Each slit acts as a source, and creates a diffraction/interference pattern, when light is transmitted through the grating. This pattern will give several maxima, called intensity maxima for different orders. For the *zeroth order*, the maxima will be given at the same location, described by the angle  $\beta$ , for all wavelengths. For the higher orders, however, the location of the maxima,  $\beta$ , varies with wavelength. Longer wavelengths, such as red light, will have a greater angle than the shorter wavelengths, such as blue light. It is worth noting that this is opposite from the effect happening in a prism, where shorter wavelengths are more refracted than the longer wavelengths.

While the diffraction grating transmits light, the *reflective grating* reflects light. The plane reflective grating may be seen as a polished surface with parallel grooves, i.e. long narrow cuts. The grating is filled with narrow parallel mirrors, with each mirror acting as a source. Thus the same interference pattern as for the transmitting grating is created when the reflective grating is exposed to light.

The *grating equation* is given as

$$n\lambda = a(\sin \alpha + \sin \beta), \quad (2.1)$$

where  $n$  is the spectral order,  $\lambda$  the wavelength,  $a$  the distance between the grooves,  $\alpha$  the incident angle, and  $\beta$  the diffracted angle of the light. This equation is based on an idealised grating, but can be used to calculate the theoretical diffracted angle in a system, and is highly useful when designing a hyperspectral imager.

The reflective surfaces may also be tilted at an angle  $\omega_b$ . This gives a *blazed grating*, where  $\omega_b$  is known as the blaze angle. The blaze angle introduces a shift of diffraction pattern away from the zeroth order over to higher orders. The grating is most efficient when

$$\alpha - \omega_b = \omega_b - \beta.$$

The light will be separated according to the grating equation when the diffraction pattern is shifted to the higher orders. This is the principle used to obtain spectral information, as the separated wavelengths are focused onto the imaging sensor in a hyperspectral imager.

### Optical diagram

The optical diagram of a spectrograph can be seen in Figure 2.4. As seen in the diagram, the light enters the front lens, and is focused through the slit. Further it is directed onto the second lens which collimates the light before it reaches the grating. The dispersive element shown in this optical diagram may be a grating together with a prism, which sorts the wavelengths so that the centre wavelength is parallel to the optical axis. The light is then separated and focused onto the image sensor by the third lens. This makes the captured image a *spectrogram*, with spectral information in one direction and spatial information from the slit in the other direction.

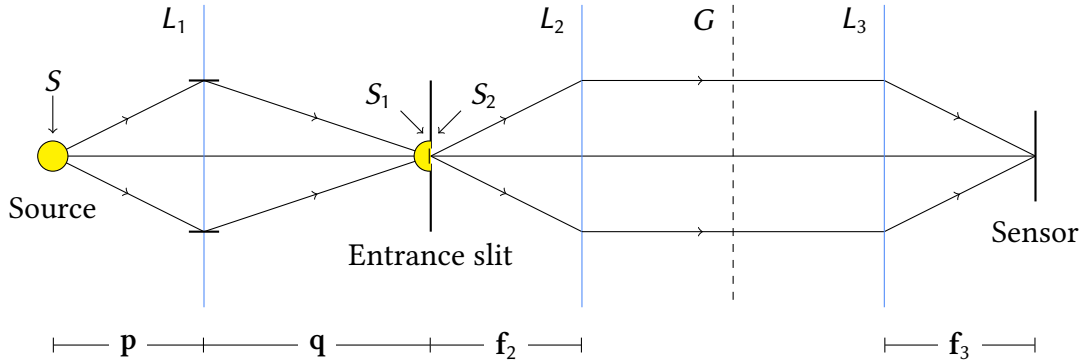


Figure 2.4: Optical diagram of a spectrograph.  $S$  is the area of the light source,  $S_1$  the area of the source image, and  $S_2$  the area of the entrance slit.  $L_1$ ,  $L_2$  and  $L_3$  are the lenses in the system, and  $G$  the grating element. Further is  $p$  the distance between object and front lens,  $q$  the distance between front lens and projected image,  $f_2$  the focal length of  $L_2$ , and  $f_3$  the focal length of  $L_3$ . Based on figure in [14].

### Bandpass

The *spectral bandpass*,  $BP$ , is defined as the recorded full width at half maximum (FWHM) of a monochromatic spectral line, and is a measure of the instruments ability to separate adjacent spectral lines in the spectrogram. An illustration of FWHM for a well aligned and a real instrument can be seen in Figure 2.5.

Spectral bandpass is calculated as

$$BP = FWHM \approx \frac{d\lambda}{dx} \times w',$$

where  $d\lambda/dx$  is the linear dispersion describing the change in diffraction angle with wavelength, and  $w'$  the exit slit width.  $BP$  can also be expressed using the entrance slit

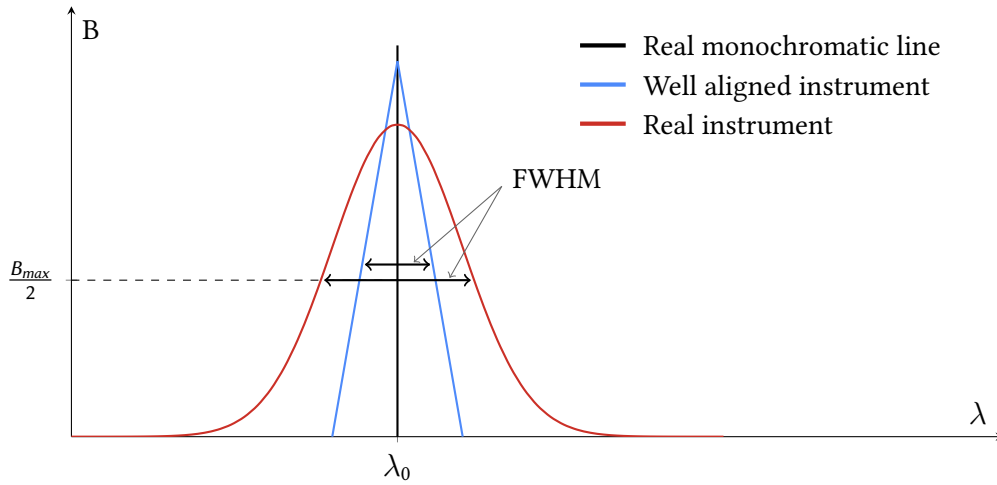


Figure 2.5: Illustration of bandpass, full width at half maximum (FWHM), for a well aligned and a real instrument. Based on illustration from [14].

width, as

$$BP = \frac{a \cos \alpha}{n f_2} \times w,$$

where  $w$  is the entrance slit width,  $a$  is the distance between the grooves in the grating,  $\alpha$  is the angle of the incident wave,  $n$  is the spectral order, and  $f_2$  the object distance.

### Geometrical extent

The *geometrical extent*, also known as etendue, characterises the ability of an optical system to accept light. It can be seen as an acceptance cone where the photons are allowed to travel, and defines how much light that can be detected by the instrument. The geometrical extent is defined as

$$G = \int \int dS d\Omega,$$

where  $S$  is the area of the emitting source and  $\Omega$  the solid angle.

### Stray light

*Stray light* can be defined as any unexpected radiation that falls onto the image plane and has an effect on the final image quality. There can be several different sources causing stray light. Light that originate from outside of the sensor's FOV, *out-of-field stray light*, is one of the major sources. Further, stray light may be separated into two classes; random and directional. *Random stray light* is typically due to scatter from different components within the system, such as mirrors or screws. This stray light will be directly proportional to the

flux density. *Directional stray light*, on the other hand, can result in more distinct errors. Some of these may be incorrect illumination due to overfilled optics, re-entry spectra of unwanted orders or stray light due to periodic machine ruling errors.

### Aberrations

In a perfect imaging system, all rays that originate from the same point in an object will cross at the same point in the system imaging plane. In real optical systems, however, this is not the case. This happens due to *aberrations*, which can be described in terms of how much a ray deviates from its desired location in the imaging plane. The desired location of the imaging points are based on first-order optics. Refraction of light follows *Snell's law*,

$$n_1 \sin \theta_1 = n_2 \sin \theta_2,$$

where the terms can be expanded so that

$$\sin \theta = \theta - \frac{\theta^3}{3!} + \frac{\theta^5}{5!} - \frac{\theta^7}{7!} + \dots,$$

where  $\theta$  is the angle measured from the normal of the boundary. For small values of  $\theta$ , the higher order terms can be neglected, and Snell's law can then be written as

$$n_1 \theta_1 = n_2 \theta_2.$$

This, however, holds only for paraxial rays. For nonparaxial rays higher order terms must be included. Including the third order term will give *third-order optics*, which introduces several monochromatic aberrations such as astigmatism and different types of distortions.

### Sensor detection

The focal plane array (FPA), the detector matrix which the image is focused onto, converts the irradiance distribution produced by the imaging optics into the electrical signal that is recorded. It consists mainly of two parts: an array of detectors, and a multiplexer. The detector array produces an electrical response, when hit by incident radiation. The multiplexer then collects the electronic response, and produces a signal with the digital representation of the detected image.

### Quantum efficiency

The *quantum efficiency*,  $QE$ , describes the spectral responsivity of each pixel in the detector. It is defined as the fraction of photons that can generate electrons detectable by the sensor. The  $QE$  can be calculated as a function of wavelength. This can further be used to characterise the sensitivity of the imager.

### Point Spread Function

The ideal wavefront exiting an optical system for a point object will be spherical in nature, and will converge to a perfect point on the focal plane. However, imperfections in the optical system stop this from happening. Aberrations cause rays to land at different locations on the focal plane, and broadens the image of the point object. Distortion may cause the magnification to change as a function of image position. Absorption decreases the transmission of the light through the system, and diffraction from the finite aperture size provides the final resolution. The actual focal plane image can be given by

$$E(x, y) = E_g(x, y) \star h(x, y),$$

where  $E(x, y)$  is the actual plane image,  $E_g(x, y)$  the true point source,  $\star$  represents a 2D spatial convolution operation, and  $h(x, y)$  is the point spread function (PSF). An illustration of the PSF can be seen in Figure 2.6.

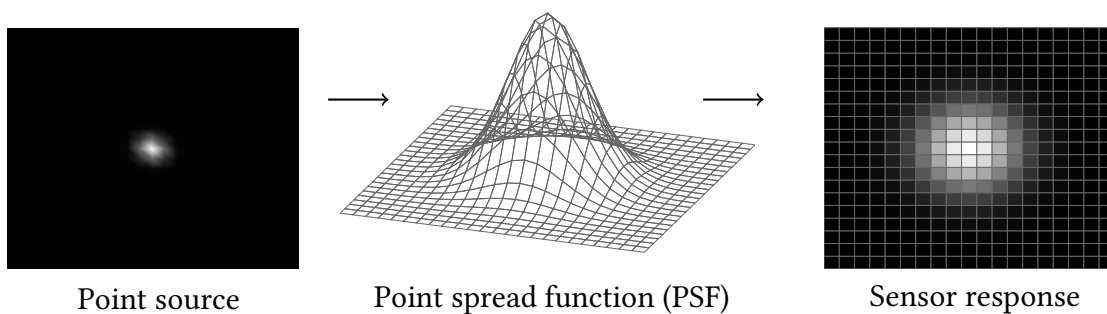


Figure 2.6: Illustration of the point spread function.

For a fuller understanding of the final optical design and performance of the system, the PSF should be characterised. This will give information about any geometrical aberrations in the system. Spatially scattered light, spatial stray light, may also be characterised by the point spread function [16].

### 2.1.3 Remote Sensing

Different techniques can be used to obtain the full hyperspectral cube when hyperspectral imagers are used in remote sensing. Two common pointing methods for doing this are pushbroom and whiskbroom scanning, as seen in Figure 2.7 and 2.8, respectively. In whiskbroom scanning, the slit is oriented in the along-track direction, and the scan happens in cross-track direction as the platform moves along-track. This allows the swath width to be decoupled from the velocity of the platform, but requires a more complex pointing system. The pushbroom concept is described below. A snapshot hyperspectral imager is a different concept where the hyperspectral cube can be acquired at one exposure. Since the snapshot imager obtains the whole cube at every exposure, the only additional parameter needed is the exterior orientation. This gives room for less geometric instabilities [17]. Another method, more applicable to multispectral imaging, is proposed in [13]. The imager has line filters on the image sensor to obtain information from different bands. This is used in combination with the pushbroom technique to obtain full spatial images with all bands. This method can be hard to extend into hyperspectral imaging due to the limited number of bands that can be fitted onto one sensor.

#### Pushbroom

The optical design described in this report is based on pushbroom HSIs. These instruments capture a spectrogram with spatial and spectral information in each frame, and requires a scanning motion to obtain the second spatial dimension to provide the full hyperspectral cube. This scanning motion is provided by the movement in the platform, when used on an air- or spaceborne platform. The slit is mounted in cross-track direction, and one line is then captured at a time. The next line is captured with new spatial information when the platform moves, as seen in Figure 2.7. These images are then stitched together to form a full spatial image, with spectral information on the third axis.

Hyperspectral imagers using the pushbroom technique offer good enough signal-to-noise ratio to be used in remote sensing, both in airborne and orbiting platforms. However, as mentioned in [18], high quality spectroscopic data is not necessarily easily obtained. The acquired spectrum may be distorted by artefacts that makes it harder to identify both spectral and spatial features. The method, however, requires a less complex pointing system than whiskbroom scanning, and the design of the imagers is less complex than for snapshot hyperspectral imagers.

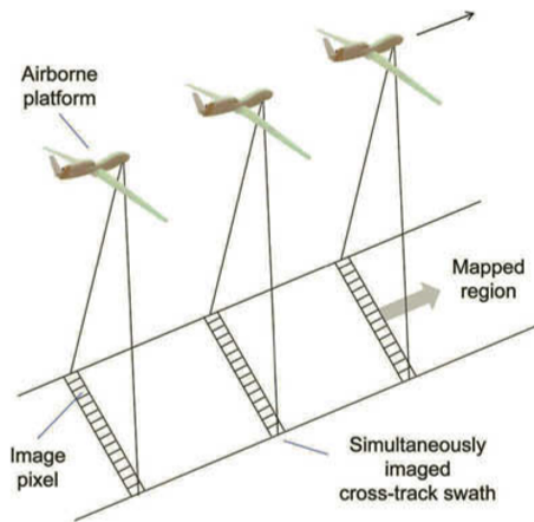


Figure 2.7: Illustration of the pushbroom scanning technique, from [1].

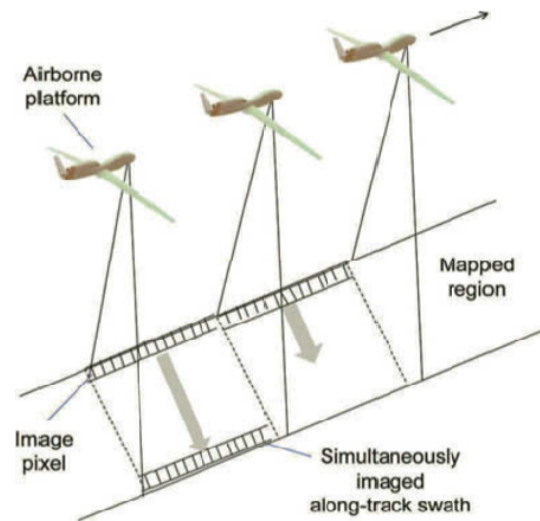


Figure 2.8: Illustration of the whiskbroom scanning technique, from [1].

### Swath width

The swath width is defined as the width of the field of view across the ground. [19]. If the FOV of the camera and distance to ground,  $z$ , are known, the swath width is given by

$$\text{swath width} = z \tan\left(\frac{\text{FOV}}{2}\right).$$

## 2.2 Calibration

Calibration is in general done to convert the measured data into physical, and more meaningful, units. This is done by comparing a known measurement, a standard, with the measurement done by the instrument that is being calibrated. In this project, spectral and radiometric calibration is performed on hyperspectral imagers. The general information about these two calibrations is presented in this section.

Instruments used in remote sensing should also be calibrated in-flight or in-orbit, in addition to laboratory calibration [12]. Only the latter is handled in this report.

Further, it is worth noting that radiometric calibration assumes that the information from the spectral calibration is known [12]. The spectral calibration must therefore be performed before the radiometric calibration can take place [14].

### 2.2.1 Spectral Calibration

In *spectral calibration*, or wavelength calibration, the relationship between wavelength and pixel position is determined. This can be achieved by using a monochromator that produces monochromatic light at controllable wavelengths, so that the response at every wavelength can be recorded. That method, however, can be impractical and also unnecessary, because the spectral-spatial distortion often will be a somewhat well-behaved function [1]. Instead, a selection of some light sources with known spectral peaks can be used to measure the response at some wavelengths, which gives enough information to derive an approximation for the wavelength and pixel position relationship.

Spectral calibration can be performed using different set-ups. Among these are calibration using spectral lamps, a monochromator, or tunable laser technology which all use known emission lines, or gas cells using known absorption lines for calibration [12]. The method in this report is calibration using spectral lamps. For this method, spectral lamps with known spectral emissions are used together with a diffuser, such as a diffuse board or an integrating sphere, to make sure the full FOV is uniformly filled with light.

The data from spectral calibration can also be used to characterise the spectral resolution of the system by finding the FWHM on the detected lines. It can also be used to investigate the smile effect, which is further described in Section 2.3.1.

### 2.2.2 Radiometric Calibration

The throughput, the usable flux at the sensor plane, depends on the input flux and the geometrical extent of the imaging system. It also depends on the quality and efficiency of the optical components used [14]. Both the throughput and efficiency of the optical components can be calculated theoretically, but for practical purposes it is more useful to calibrate the instrument against a source of known intensity to obtain the number of digital counts, or digital number (DN), by measuring the reference source. This is known as *radiometric*, or sensitivity, calibration. A diffuse reflective surface is also needed to make sure that the instrument's FOV is illuminated uniformly.

The aim of the radiometric calibration is to correctly convert the raw data from DN to radiance or reflectance, which are much more physically meaningful units. This calibration can also remove some of the deviations caused by the hyperspectral sensor itself, and correct for some of the atmospheric effects if calibrated in-flight or in-orbit [17]. Usually

the relationship is assumed to be linear, giving

$$\begin{aligned} L(\lambda) &= K \cdot C \\ C &= C' - b_0, \end{aligned} \tag{2.2}$$

where  $L(\lambda)$  is the radiance as a function of wavelength,  $K$  is the calibration factor,  $C$  is sensor counts from detected radiance,  $C'$  the total sensor count, and  $b_0$  the *dark current*, which is the number of counts present when there is no light [20]. The goal of the radiometric calibration is then to determine the calibration coefficient  $K$ , and use the measured count  $C'$  to convert to the correct radiance value at each pixel,  $L(\lambda_{i,j})$ . The dark current must either be characterised before the radiometric calibration can take place, or be made a part of the radiometric calibration procedure.

Radiometric calibration can be divided into two categories, *absolute* radiometric calibration, and *relative* radiometric calibration. This report focuses on the absolute radiometric calibration, which uses a known source to convert from the sensor output into absolute quantities. The relative radiometric calibration would be to calibrate the imager by using observations from the same imager at different points in time, and compare pixels to improve the image quality and uniformity [12].

To perform radiometric calibration, an irradiance standard lamp-integrating sphere, a standard detector-integrating sphere, a spectral radiometer-monochromatic parallel light, or a standard detector-diffuser, are among others equipment that can be used [12]. The method used in this report is the irradiance standard lamp-integrating sphere set-up, and is explained further in Section 3.3. The data from radiometric calibration can also be used to characterise the linearity of the sensor response, and the stability of the response [12]. If the detector suffers from nonlinearities in the response, this nonlinearity should be characterised and corrected before the radiometric calibration is performed. [21]

### Traceability

*Traceability* is the possibility to trace the measurement back to a trustworthy reference of the measured quantity. Spectral standard light sources might emit light at specific wavelengths due to fixed physical principles. But radiance light sources need to be calibrated with respect to primary standards before they can be used for radiometric calibration. Primary standards are operated and provided by national meteorological institutes such as the National Institute of Standards and Technology (NIST) [2]. A lamp certificate should therefore be given as a part of the information about the lamp used for radiometric calibration.

## 2.3 Characterisation

Characterisation of the imager may include characterising spectral and spatial misregistration by either finding the PSF or by other methods, detect the polarisation sensitivity of the sensor, second order effects from the grating, spatial and spectral stray light, noise in the system, and so on. In this project, characterisation of spectral and spatial misregistrations are in focus. This section discusses why and how these errors occur and affects the system, and presents some earlier research on how to detect and correct for these effects.

### 2.3.1 Spectral and Spatial Misregistrations

Hyperspectral imaging sensors often suffer from spectral and spatial misregistrations due to aberrations and misalignments in the optical system. These effects may distort the spectral signatures of the targeted object, thus reducing the detection and classification accuracy [22]. Furthermore, for remote sensing systems these properties may change after launch, which makes in-flight or in-orbit correction of these effects an important issue that should be handled [23]. This report focuses on laboratory characterisation and correction, but in-orbit correction should also be made a part of future work.

There are several types of spectral and spatial misregistrations. An illustration of some of these can be seen in Figure 2.9. In an ideal system, all the lines in the figure should be straight and follow the grid. The circles represent the point spread function. The shape and size of the PSF may vary as a function of wavelength, but for the same wavelength, it should ideally be the same size and shape. The letters  $B$ ,  $G$ , and  $R$ , represents short, middle and long wavelengths within the optical range, respectively.

As mentioned in [24], a typical spectral misregistration is *smile*, which is a change in the central wavelength in a spectral channel as a function of the slit height. This can be seen as a bent line in the spectrogram. Furthermore, a typical spatial misregistration is *keystone*, which is a change in the position of the same spatial pixel in the scene, as a function of wavelength. This effect makes the spectrogram look a bit skewed. These effects are shown in Figure 2.9. The figure also shows two other effects. The  $G$  column shows a variation of the width of the points, so the PSF can vary with spatial location in the image. The bottom row shows an increasing height in the PSF as a function of wavelength. This can be caused by diffraction, and can be hard to avoid in a diffraction based system [18]. Ideally, all of

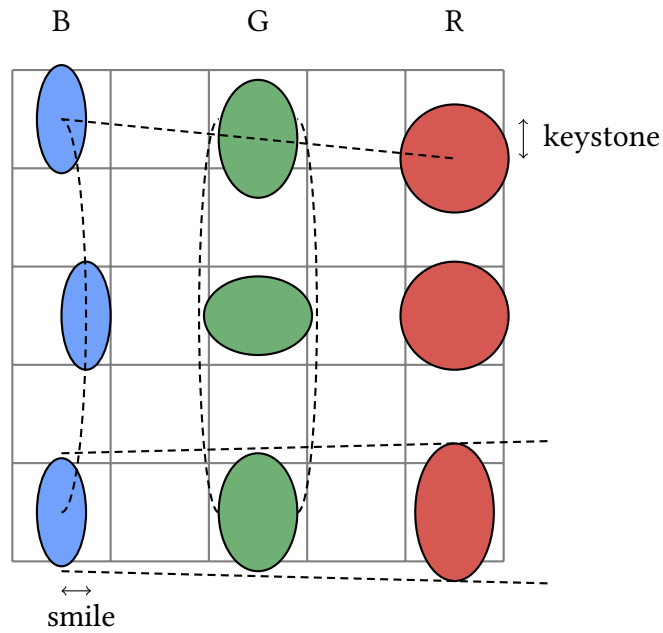


Figure 2.9: Illustration of different types of misregistrations that may occur in a pushbroom hyperspectral imager. Inspired by illustration in [18].

these effects should be characterised, which can be done by measuring the PSF. To measure the PSF along the slit to cover all spatial positions for all wavelengths requires a possibly complex and dedicated set-up. An example of such a set-up can be found in [25], using line spread functions measured in different directions to reconstruct the PSF. The focus in this report, however, is to detect mainly the smile and keystone distortions, while a set-up for measuring the PSF will be a part of the future work of this project.

A metric for characterising coregistration errors, including smile and keystone, was proposed in [26]. The metrics are essentially the integrated difference between the point spread functions, and it is shown that they correspond to an upper bound on the error in the image data. Using this metric, two commercial hyperspectral imagers were tested and compared in [27]. This showed that characterising imagers using the proposed metric made it possible to compare the performance of hyperspectral imagers more thoroughly, giving better estimates on the differences.

### 2.3.2 Detection Methods

In [28] it was shown that classical 2D camera characterisation methods, to detect geometrical features, are not sufficient for characterising 1D imagers. Further a two-step method for characterising a line scan imager using a 2D structure with skewed lines in different orientations, to give several interception points, was described. A similar pattern, but in 3D, was printed onto two parallel planes in [29]. Geometry was again used to calculate the coordinates of the corresponding intersection points. These points were further used to obtain inner and outer orientation parameters by a standard calibration procedure based on bundle block adjustment principle, which is one of the most common approaches for characterising a line sensor in close-range applications [30]. Again, a similar calibration model was given in [31]. The same pattern was used and position of the intersection points were again calculated using geometry, but the pattern was now placed in two perpendicular planes. An illustration of the pattern used can be seen in Figure 2.10. In [32], this characterisation procedure was extended further to include characterisation of radial distortion in the system. These methods seems like a good way for characterising a line imager. But for remote sensing instruments the pattern would have to be many metres in length, with an even greater distance between the imager and the characterisation target for the pattern to be in focus. This method will therefore neither be used nor investigated any further in this report.

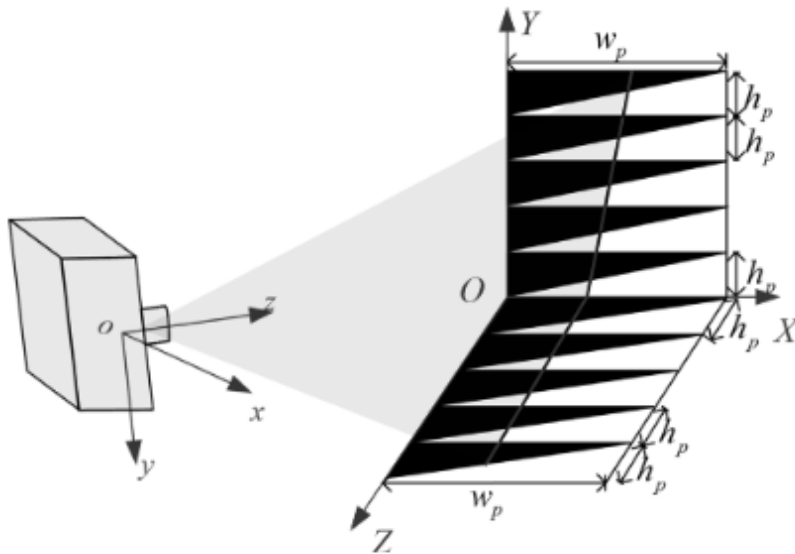


Figure 2.10: Pattern used for calibration in [31].

The calibration facility for airborne imaging spectrometers, CHB at DLR, uses a collimator set-up for geometric measurements, as described in [11] and [33]. A schematic sketch of the set-up can be seen in Figure 2.11.

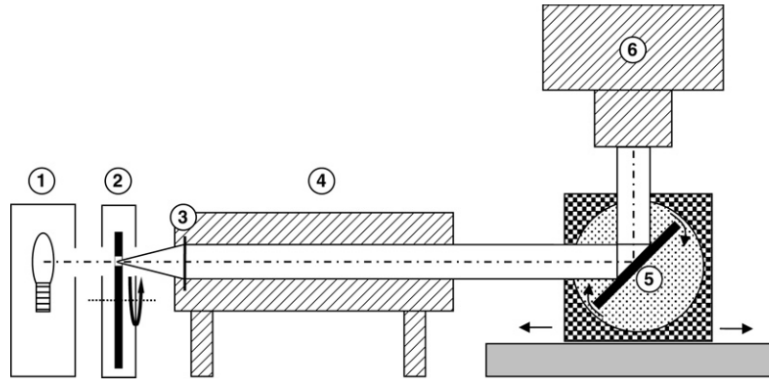


Figure 2.11: Set-up for geometric measurements at CHB. 1) lamp, 2) slit in turnable wheel, 3) parabolic mirror, 4) collimator, 5) folding mirror, 6) sensor. Illustration from [11].

For across-track measurements, the slit is mounted tangentially on the wheel so that an illuminated line is formed on the detector array by different wavelengths. Measurements are then performed by moving the line using the folding mirror. For along-track measurements the slit is mounted radially on the wheel, and measurements are obtained by turning the slit wheel. This can be used to find the line spread function, among others, which can further be used to estimate the point spread function, as done in [25]. A smaller and simplified version of the collimator set-up is proposed in this project, and is further described in Section 3.1.2.

As mentioned in [34], both spectral and spatial misregistrations should be detected simultaneously, since the imager projects spectral information along the horizontal axis of the sensor, and spatial information along the vertical axis at the same time.

### 2.3.3 Correction Methods

Spectral and spatial misregistrations caused by lens distortions, misalignments and so on, can be corrected in hardware by changing to higher quality lenses with less distortions, making the whole imaging system better aligned etc. This works for larger errors, but when the errors get smaller these corrections are harder to make in the hardware. Developing a perfect imaging system is by no means practical, if it is possible at all. Some distortions will most likely always be present. In [24], resampling, thus making the corrections in software,

was proposed as an alternative method for correcting keystone. They found that better corrections could be made by using this method instead of trying to correct the keystone effects in hardware, for high-resolution sensors. They also suggest that the same method may be used to correct for smile effects.

According to [18], smile and keystone can be minimised using optimisation. Two or three wavelengths may be chosen from the desired spectral range, and the coordinates of the intersection point between the rays and the image plane can be found. The desired difference in these coordinates can then be set to zero as a constraint, and be given an appropriate weighing factor. To calculate a more exact amount of smile or keystone in the system, the PSF centroid locations should be used instead of the intersection points. Other constraints that can be used in the optimisation function are minimisation of the PSF width and height differences for each wavelength. This method, however, is mainly used when designing the optical system, to optimise the design.

In [22] and [23], an image registration method based on phase correlation was proposed and tested on hyperspectral data from the Hyperion instrument on the EO-1 satellite. It was shown that this method can be used to detect spectral and spatial misregistrations, also postlaunch. To modify the spectral signatures for correction, cubic spline interpolation was used.

In [34], a method for correcting both smile and keystone simultaneously using an adaption of a geometric control point calibration (GCP), was proposed. The method maps distinct points in an image to known locations using a 2D quadratic polynomial distortion model given by

$$\begin{aligned} x &= a_{00} + a_{10}x_{ref} + a_{01}y_{ref} + a_{11}x_{ref}y_{ref} + a_{20}x_{ref}^2 + a_{02}y_{ref}^2 \\ y &= b_{00} + b_{10}x_{ref} + b_{01}y_{ref} + b_{11}x_{ref}y_{ref} + b_{20}x_{ref}^2 + b_{02}y_{ref}^2, \end{aligned}$$

where  $x$  and  $y$  are the measured coordinates,  $x_{ref}$  and  $y_{ref}$  the reference coordinates, and  $a$  and  $b$  are the model coefficients.

It is also mentioned in [34] that without GCP correction, individual calibrations must be applied to every pixel of the FPA because of possible non-linearity across the FPA. If GCP is used to correct the FPA image, however, single-wavelength and distance calibrations are sufficient to correct all the pixels. This reduces the overall complexity of the calibration procedure considerably.

## 3 | Methods

This chapter describes the different calibration and characterisation set-ups and procedures, and gives detailed information about the equipment used.

As mentioned in the previous chapters, calibration and characterisation are distinguished by their goals. The calibration identifies parameters holding metadata, such as the pixel to wavelength relationship in spectral calibration, and sensor count to radiance in radiometric calibration. It will use known sources for comparison, and the results are used to convert raw sensor data into physically meaningful units. The characterisation will identify sensor parameters describing the capabilities of the system itself. It will identify limits, such as upper and lower limits of the dynamic range, and other features in the system. The results from the characterisation will also be used to identify distortions, such as smile and keystone, in the system.

There is assumed no atmospheric attenuation during the laboratory calibration and characterisation procedures. The distance between imager and light source is small, and there should therefore be close to no effect on the results when calibrating in the lab. Should the distance increase however, such as for in-flight or in-orbit calibration, handling this effect should be a part of the procedure.

### 3.1 Equipment

The integrating sphere used is an ISS-30-VA integrating sphere from Gigahertz Optik, as shown in Figure 3.1. For the radiometric calibration, the integrating sphere is used with the power turned on, using the lamp in the sphere as the light source. The lamp certificate of this lamp can be found in Appendix A. It is worth noting that a log of hours used for the lamp has not been found, so there is no guarantee the lamp is still within its specification. For the spectral calibration, however, the sphere is only used as a uniform diffuser, while the light sources are spectral calibration lamps.

The spectral calibration lamps produce narrow, intense lines from the excitation of the gas, or vapour, inside. The lamps used in this calibration are based on argon, krypton, and xenon gas, as well as mercury vapour. The mercury lamp contains argon gas, and therefore needs

two minutes of warm-up time for the mercury vapour to dominate the discharge. It is also worth noting that the mercury lamp has an intense ultraviolet (UV) output profile, and UV protective eyewear is recommended when operating the lamp. An image of the spectral calibration lamps used is shown in Figure 3.2. The typical spectra and wavelength values of the lamps can be found in [35]. The calibration lamps are all of the type called pencil style calibration lamp, due to their thin shape and small size.

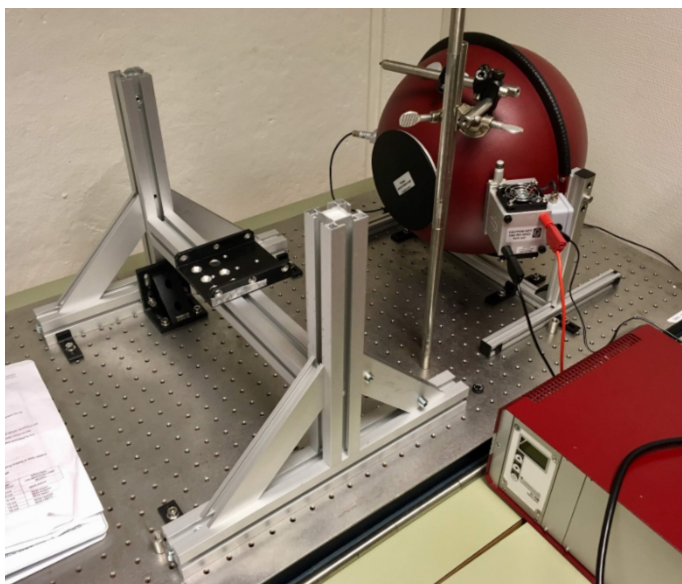


Figure 3.1: Integrating sphere, ISS-30-VA from Gigahertz Optik.



Figure 3.2: Spectral calibration lamps; 6030 (Ar), 6031 (Kr), 6033 (Xe), and 6065 (Hg).

Two hyperspectral imagers are calibrated and characterised in this report, the HSI V4C [36] and the HSI V6 [37]. These are described further in Section 3.1.1.

The collimator set-up proposed for detecting keystone is presented in Section 3.1.2. It consists of a Zeiss Makro-Planar 100 mm f/2 lens with Nikon mount that collimates the light, and a lens cap with transparent top pattern. An image of the parts can be seen in Figure 3.6.

An overview of the equipment used, can be seen in Table 3.1. Other equipment such as power supply, optical table, mounting equipment etc. will not be described any further.

Table 3.1: List of equipment used.

Equipment	Specifications
Integrating sphere	ISS-30-VA, [38] Including X1-RM optometer and LPS-100-RM lamp power supply
Spectral lamp: Argon (Ar)	Model no.: 6030, [39]
Spectral lamp: Krypton (Kr)	Model no.: 6031, [40]
Spectral lamp: Xenon (Xe)	Model no.: 6033, [41]
Spectral lamp: Mercury (Hg(Ar))	Model no.: 6035, [42] Note: UV radiation
Power supply, spectral lamps	Newport 6044 AC Lamp Power Supply, [43]
Optical table	Optical table from Technical Manufacturing Corporation (TMC)
Dark room	Optical lab at NTNU, room A492C
Mounting equipment	
Collimator lens + lens hood	Zeiss Makro-Planar 100 mm f/2 lens with Nikon mount, with the belonging lens hood
Stripe pattern	3D printed stripe pattern, made to fit the collimator lens. Height: 46.5 mm (corresponds to Nikon SLR focal length) Thin stripe pattern: 26 slits, 8 mm $\times$ 0.5 mm Thick stripe pattern: 8 mm $\times$ 1 mm, separated by 1 mm
Hyperspectral imagers	HSI V4C and HSI V6

### 3.1.1 HSI V4C and HSI V6

There are two hyperspectral imagers used in this report, the HSI V4C [36] and the HSI V6 [37], which can be seen in Figure 3.3 and 3.4, respectively.

The imagers are both developed by Fred Sigernes at UNIS, with the HSI V6 being the most recent version of the two. The specifications of the imagers can be seen in Table 3.2. They are both based on the same optical design, and uses camera heads from Imaging Development Systems (IDS), but they have different lenses and specifications. A general optical diagram for both imagers can be seen in Figure 3.5.



Figure 3.3: Image of the HSI V4C.



Figure 3.4: Image of the HSI V6.

Table 3.2: Specifications of the HSI V4C and HSI V6.

Part	HSI V4C	HSI V6
Camera head	uEye UI-3360CP-NIR-GL	UI-3060CP-M-GL Rev.2
Sensor type	Monochrome CMOS	Sony IMX174, CMOS
Spectral range	297.5 - 1005.5 nm	400-800 nm
FWHM	1.4 nm	approx. 3.3 nm
Grating	600 grooves/mm transmission grating	300 grooves/mm transmission grating
Slit height	3 mm	3 mm
Slit width	25 $\mu\text{m}$	50 $\mu\text{m}$
Slit height magnification	1.28	none

The HSI V4C is designed so that the centre output wavelength is  $\lambda_c = 552.5$  nm, following the grating equation, Equation 2.1, for the first spectral order ( $k = 1$ ),

$$\lambda = \left(\frac{a}{k}\right) \cdot \sin \beta,$$

where the groove spacing is  $a = 1666.67$  nm, and the diffraction angle  $\beta = 19.36^\circ$ .

### 3.1.2 Collimator Set-up

The collimator set-up is designed for characterisation of the keystone effect in the system. The background motivation for making this collimator set-up is described in Section 2.3. A collimator-set up is also used at DLR for geometric measurements, as described in Section 2.3.2. This set-up, however, includes a turnable wheel and several other components, and is designed for characterising more effects than just keystone. A simplified version of a collimator set-up is therefore presented in this report.

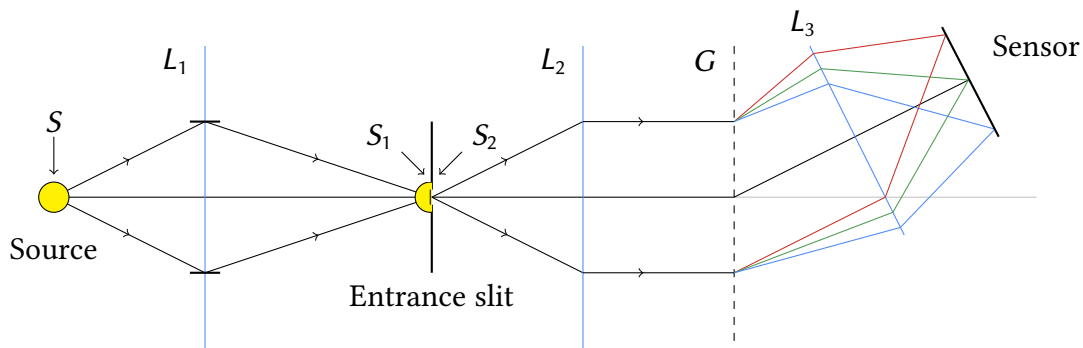


Figure 3.5: Optical diagram of HSI V4C and V6.  $S$  is area of the light source,  $S_1$  the area of the source image, and  $S_2$  area of the entrance slit.  $L_1$ ,  $L_2$  and  $L_3$  are the lenses in the system, and  $G$  the transmission grating.

The idea of using a lens objective and a 3D printed pattern belongs to Fred Sigernes, who also designed the hyperspectral imagers used in this report. The lens objective used is a Zeiss Makro-Planar 100 mm f/2 lens with Nikon mount. The 3D printed part is made so that the striped pattern is at a distance corresponding to the focal length behind the lens. The incoming light from the front side of the collimator lens is then focused onto the striped area, where the sensor normally would be located. Correspondingly, if the striped pattern is illuminated from the other side, the pattern as if looking at it from an infinite distance would be seen when looking into the front lens. The front is assumed to be set to infinity.

Since the imagers in this report will be used for remote sensing, they will have focus set to infinity. Using this set-up will allow the imagers, with focus set to infinity, to look at the striped pattern at a close distance with the pattern still being in focus. This sums up the goal of using this set-up.

An image showing the collimator set-up parts can be seen in Figure 3.6, and the striped pattern is shown in Figure 3.7. The 3D printed part is fastened onto the mounting side of the lens objective, and the lens hood attached on the front side of the lens, as shown in the figure. The lens hood is used to minimise extra light from the surroundings when acquiring images through the front lens. Figure 3.8 shows the optical diagram of the collimator set-up. The hyperspectral imager is placed right in front of the lens objective to obtain an image of the striped pattern. A light source, preferably with a continuous spectrum to capture the pattern at all wavelengths, is placed behind the 3D printed pattern. Other light sources may also be used, but lamps with only few spectral lines will give less information to detect keystone in the image.



Figure 3.6: The collimator set-up consisting of a Zeiss Makro-Planar 100 mm f/2 with lens hood, and a 3D printed lens cap with top pattern.

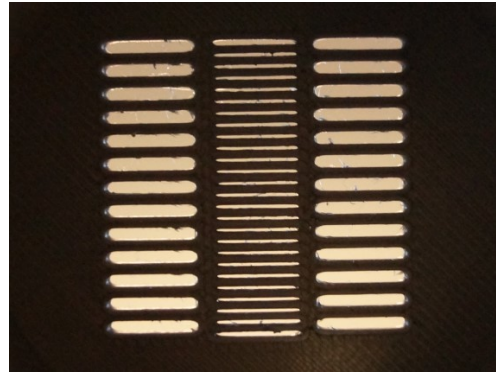


Figure 3.7: The 3D printed pattern, imaged with a Sony  $\alpha$  57.

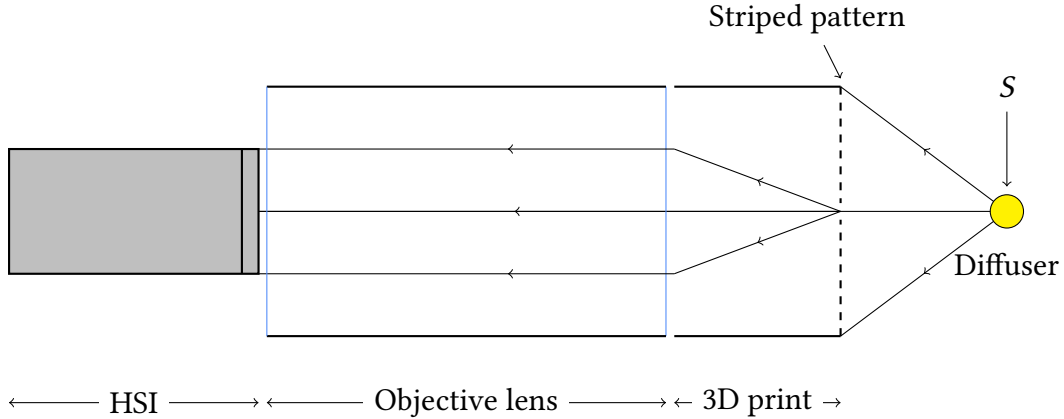
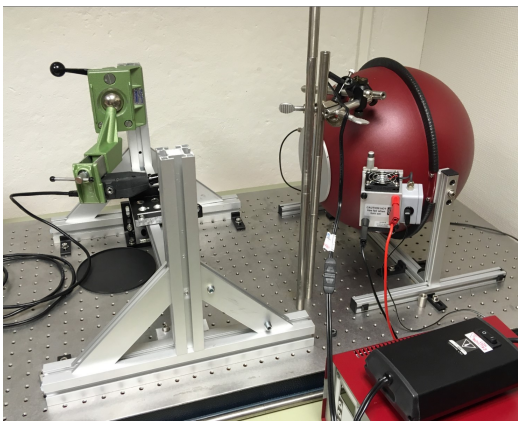


Figure 3.8: Optical diagram of the collimator set-up, showing the path for light entering the middle slit.

## 3.2 Spectral Calibration

The lamps used for this spectral calibration are four spectral lamps, based on argon, krypton, xenon and mercury, as described in Section 3.1. An image showing the experimental set-up can be seen in Figure 3.9.

Before the procedure started, the imager was mounted in front of the integrating sphere. The spectral calibration lamp was then placed in the inlet of the integrating sphere, and connected to the power supply. All other light, except light from the laptop used for controlling the camera, was turned off. The spectral lamp was then turned on. The first image taken was analysed to verify that the image was not over- or underexposed. If needed,



*Figure 3.9: Set-up for spectral calibration. The spectral lamp is placed in an inlet on the integrating sphere, so that uniformly distributed light is achieved at the outlet of the sphere.*



*Figure 3.10: Light from the outlet of the sphere during spectral calibration with the 6031 Krypton lamp.*

parameters were adjusted, and a new test image taken. When the test image was properly exposed, the calibration started. An image taken of the set-up during calibration with the krypton lamp is shown in Figure 3.10. The intensity is quite low, so the settings should be adjusted so that the highest peaks are close to being overexposed, to maximise the signal obtained.

Spectral calibration was performed several times, on different hyperspectral imagers, with different settings. The gain was kept at zero (no gain) and the binning at one (no binning) at all times. The full area of interest (AoI) was calibrated. Each dataset contains about 20 images in the form of spectrograms.

The wavelength pixel relation is assumed to be

$$\lambda \approx a_0 + a_1 \cdot p + a_2 \cdot p^2, \quad (3.1)$$

where  $\lambda$  is the wavelength in nanometres and  $p$  the pixel value. The result after the data has been analysed will be the constants  $a_0$ ,  $a_1$  and  $a_2$  describing this relation [14].

### 3.3 Radiometric Calibration

The integrating sphere used for radiometric calibration in this project is described in Section 3.1. The inside of the sphere acts as the diffuse multiple reflecting surface, making the light at the outlet uniform.

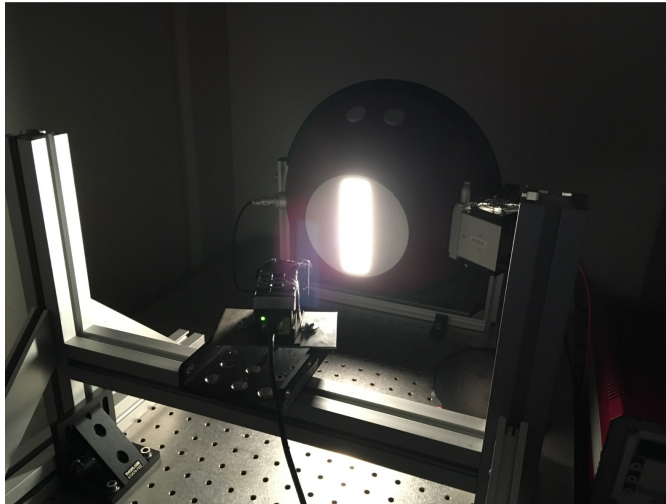


*Figure 3.11: Set-up for radiometric calibration.*

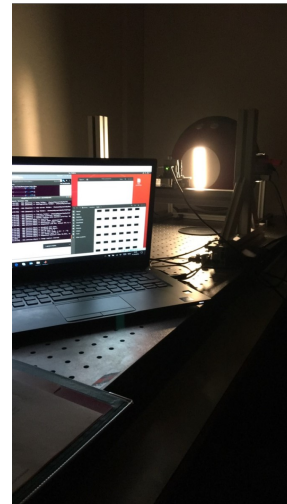


*Figure 3.12: Some light pollution from the laptop.*

The radiometric calibration set-up can be seen in Figure 3.11. The light source is quite strong, so the light pollution from the laptop screen, as seen in Figure 3.12 is assumed to have no effect.

As mentioned in Section 2.2.2, the relationship between sensor count and radiance is described by Equation 2.2. The dark current,  $b_0$ , must either be characterised before the radiometric calibration can take place, or be made a part of the radiometric calibration procedure. In this project, it will be a part of the calibration procedure. The radiometric calibration therefore consists of two steps: finding the dark current,  $b_0$ , and then finding the calibration coefficient  $K$  to obtain the full relation between sensor counts and radiance.

To obtain the dark current,  $b_0$ , the imager was placed in the dark room with all lights turned off, except the light from the computer used to control the camera. The lens cap was kept on. Images were then taken with different exposure times to obtain several estimates for the dark current per second. The gain was kept at zero (no gain) and the binning at one (no binning) at all times. The full AoI was calibrated.

Before the procedure to find  $K$  started, the integrating sphere was turned on. The radiance from the lamp may vary a bit before it is fully warmed up, so the lamp should be allowed 10-20 minutes to achieve stable radiance before use. The imager was then placed in front of the outlet of the integrating sphere, at a distance so that the full FOV was illuminated. All other light, except light from the laptop used for controlling the camera, was turned off when the calibration lamp was ready. The first image taken was analysed to verify that the image was not over- or underexposed. If needed, parameters were adjusted, and a new test image taken. The calibration started when the test image was well exposed. Images were then again taken with different exposure times to obtain several estimates for radiance per second. This is done since the count rate as a function of exposure time not necessarily is linear, as mentioned in [14]. The gain was kept at zero (no gain) and the binning at one (no binning) at all times and the full AoI was calibrated here as well.

## 3.4 Characterisation

The characterisation procedure in this report focuses on detecting smile and keystone effects in the system. Other effects may also be characterised. These include the point spread function, spectral bandpass, dark current, polarisation sensitivity, second order effects from the grating, spatial and spectral stray light and the noise in the system. The dark current is found as a part of the radiometric calibration procedure, which is described in Section 3.3. The spectral bandpass will be calculated using data from the spectral calibration. The other effects mentioned are not treated in this report.

It is worth noting that neither the HSI V4C nor the V6 have any filters to filter out second order effects from the grating. The imagers used are not sensitive to UV light below 400 nm due to absorption by the glass lenses used, but second order effects may appear or blend in above 800 nm [36].

### 3.4.1 Spectral Misregistrations (Smile)

Smile is detected using the data from the spectral calibration. For each row in the image the spectral peaks are detected. Smile causes these peaks to have different pixel positions, giving an effect that looks like a bent spectral line in the spectrogram, as described in Section 2.3.1. The position of the peaks for each row will therefore be compared, and used to make a function compensating for the this effect, thus correcting for the smile effect.

### 3.4.2 Spectral Bandpass

Spectral bandpass is estimated using data from the spectral calibration. The full width of the peak at half maximum is calculated for several peaks, and an average of bandpass for the peaks calculated to find an estimate of the spectral bandpass in the imager.

### 3.4.3 Spatial Misregistrations (Keystone)

Keystone will in the future be detected using the collimator set-up described in Section 3.1.2. The pattern will show up in the spectrogram as horizontal lines. The lines may appear skewed due to the keystone effect, as the position of the lines may depend on wavelength. This will give the lines a different pixel position within each column in the image, as described in Section 2.3.1. The position of the lines within each column will therefore be recorded and compared, and used to make a function compensating for the this effect, thus correcting for the keystone effect.

## 4 | Results and Discussion

The first goal of this project was to set up spectral and radiometric calibration procedures, and calibrate hyperspectral imagers using the existing equipment at NTNU. Both spectral and radiometric calibration procedures were designed, and the calibrations performed on the HSI V4C and HSI V6. The data collected will further be used for the analysis that is required to finalise the calibration procedures. The spectral calibration data will also be used for spectral characterisation of the system. Results from the spectral calibration are described in Section 4.1, and the results from radiometric calibration in Section 4.2.

The second goal was to investigate a method for detecting smile and keystone effects in the system, and further correct these effects. A short literature review was done on existing detection and correction methods of these effects in Section 2.3.2 and 2.3.3, respectively. In Section 4.3.1, results are shown for detecting and correcting smile using the data collected during spectral calibration. For detecting the keystone effect, it was found that a set-up providing a pattern at an infinite distance was needed. To achieve this, a collimator set-up was designed and built, as described in Section 3.1.2.

Further it was found that the data collected during spectral and radiometric calibration can be used to characterise other effects in the system, such as spectral bandpass, the dynamic range, and linearity of the sensor, among others. Spectral bandpass was estimated in this report, and the result of this characterisation can be found in Section 4.3.2.

### 4.1 Spectral Calibration

Spectral calibration was performed using four spectral lamps, as described in Section 3.2. The calibration was done on both the HSI V4C and HSI V6. An overview of the data obtained during spectral calibration can be seen in Table 4.1.

The data was analysed using a Python script developed by the NTNU SmallSat team. The script uses only data obtained with the argon and mercury lamps, but can be extended to include data from all four calibration lamps. The reference peaks used are chosen among the useful wavelengths for the calibration lamps, given in [35]. The selected peaks can be seen in Table 4.2.

Table 4.1: Overview of a selection of the datasets obtained from spectral calibration. Only varied parameters such as frames per second (FPS) and exposure time (EXP), given in ms, are noted under settings.

Dataset (no.)	Date	HSI	Lamp	Settings
SP1	02.10.2018	HSI V4C	Ar	FPS=2, EXP=200
SP2	02.10.2018	HSI V4C	Ar	FPS=10, EXP=100
SP3	02.10.2018	HSI V4C	Hg(Ar)	FPS=2, EXP=200
SP4	02.10.2018	HSI V4C	Hg(Ar)	FPS=10, EXP=100
SP5	02.10.2018	HSI V4C	Kr	FPS=2, EXP=200
SP6	02.10.2018	HSI V4C	Kr	FPS=10, EXP=100
SP7	02.10.2018	HSI V4C	Xe	FPS=2, EXP=200
SP8	02.10.2018	HSI V4C	Xe	FPS=10, EXP=100
SP9	07.11.2018	HSI V6	Ar	FPS=5, EXP=100
SP10	07.11.2018	HSI V6	Hg(Ar)	FPS=5, EXP=30
SP11	07.11.2018	HSI V6	Kr	FPS=5, EXP=100
SP12	07.11.2018	HSI V6	Xe	FPS=1, EXP=600

As mentioned in Section 3.2, the results from the spectral calibration will be the spectral calibration coefficients  $a_0$ ,  $a_1$  and  $a_2$  that describes the wavelength pixel relation in Equation 3.1. The script finds the polynomial fit coefficients that match the reference peak wavelength values to the position of the peaks found in the calibration data. These polynomial fit coefficients correspond to the final calibration coefficients  $a_0$ ,  $a_1$  and  $a_2$ . The results from analysing some of the datasets described in Table 4.1 can be seen in Table 4.3. The number of pixels used when calculating the spectral range were 2048 and 2056 pixels for the HSI V4C and V6, respectively. For simplicity, only one horizontal line in the spectrum was analysed. This line was held constant at line number 200 and 500, in the vertical direction, for the HSI V4C and V6, respectively.

From the imager specifications in Table 3.2, it can be seen that the expected spectral range for HSI V4C is 297.5-1005.5 nm and 400-800 nm for the HSI V6. The results from the spectral calibration shows that the spectral range of the HSI V4C is slightly less than expected, being approximately 355-1040 nm. Both the minimum and maximum values are higher than expected. This could indicate that either the transmission grating or the focusing lens between the grating and the sensor is at a slightly different angle than planned for. The spectral range of the HSI V6 is higher than expected, with a range of 378-851 nm.

Table 4.2: The chosen reference peaks for argon and mercury used in the spectral calibration.

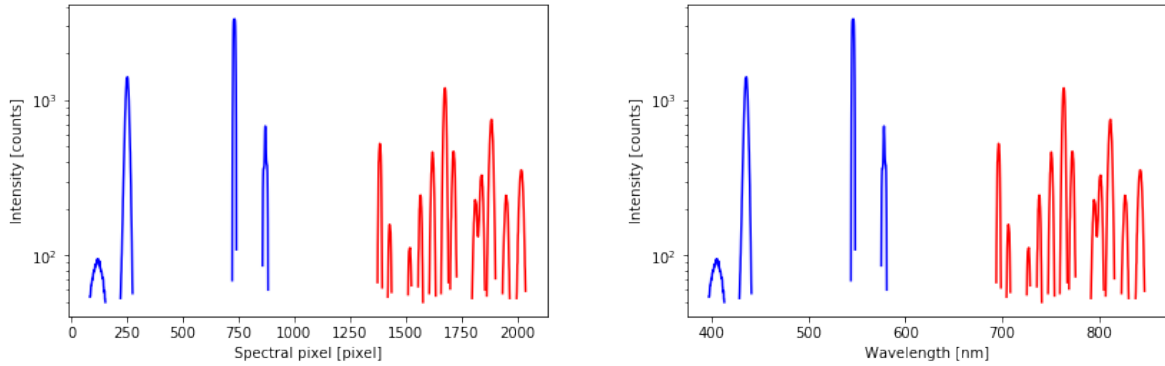
Lamp	Wavelength [nm]	Lamp	Wavelength [nm]
Hg(Ar)	404.66	Ar	751.46
Hg(Ar)	435.84	Ar	763.51
Hg(Ar)	546.07	Ar	772.38
Hg(Ar)	576.96	Ar	794.82
Ar	696.54	Ar	811.53
Ar	706.72	Ar	826.45
Ar	727.29	Ar	842.46
Ar	738.4		

Table 4.3: Polynomial fit coefficients obtained from analysing spectral datasets.

HSI	Datasets	Polynomial fit coefficients	Spectral range
V4C	SP1 and SP3	$a_0 = 358.6, a_1 = 0.3409, a_2 = -3.338 \cdot 10^{-8}$	358.6 - 1056.6 nm
V4C	SP2 and SP4	$a_0 = 354.1, a_1 = 0.3560, a_2 = -1.381 \cdot 10^{-5}$	354.1 - 1032.5 nm
V6	SP9 and SP10	$a_0 = 378.9, a_1 = 0.2295, a_2 = 3.221 \cdot 10^{-7}$	378.0 - 851.2 nm

As seen in Table 4.3, the coefficients found for HSI V4C are not equal when using different datasets. The result from datasets SP1 and SP3 gave a slightly longer range, 19.6 nm longer, with both higher minimum and maximum values than the results from datasets SP2 and SP4. The only parameters changed were the exposure time and number of frames per second, as seen in Table 4.1. This should not affect the position of the spectral peaks. The difference in spectral range values could be due to modelling errors. In that case, a better model should be made. Investigating and correcting the cause of differences in the spectral range, will be a part of future work.

One of the steps of the data analysis is to isolate the peaks from the background noise. This is done by setting a threshold parameter,  $\varepsilon$ , symbolising the maximum noise, and discarding data below this threshold. Figure 4.1 shows an example of how the calibration changes the x-axis from pixel number to wavelength value, after calibration of the HSI V6 data. The thresholding is visible in Figure 4.1, as only the peaks above the thresholding value are plotted. It is worth noting that  $\varepsilon$  had to be a much higher value for the HSI V6 data, which may indicate a higher noise floor in this sensor.



(a) Before calibration, x-axis shows pixel number. (b) After calibration, x-axis shows wavelength.

Figure 4.1: Peaks from spectral calibration at line 500 in spectrograms from dataset SP9 and SP10. Red peaks are from the argon lamp, blue peaks from the mercury lamp. Only peaks above the threshold value are shown.

When analysing the data, only one of the collected frames in the dataset was used, as this is only a preliminary characterisation method. To improve the analysis, several images within the same dataset, as well as data from several datasets, should be analysed. Further, they should give an averaged value for the spectral calibration coefficients as the result of the analysis, preferably with an uncertainty estimate for each coefficient.

## 4.2 Radiometric Calibration

The radiometric calibration was performed as described in Section 3.3. For the first part of the procedure, obtaining data to characterise the dark current, the HSI V6 was used. For the second part of the calibration, collecting data with the known light source, the HSI V4C was used. An overview of the data obtained for the first part, finding the dark current, can be seen in Table 4.4. The datasets from the second part of the radiometric calibration are shown in Table 4.5.

For the dark current analysis, a small number of counts varying for each pixel are expected. As a preliminary analysis of the dark current data from the HSI V6, lines from different datasets with different exposure times were plotted together, as seen in Figure 4.2. It can be seen that the dark current registered varies between 2 and 14 counts in line 500 in these spectrograms. Different lines were plotted, and the counts varied between 0-16 counts for lines around 600, and 5-13 for lines further out, such as 200. These numbers are within the range of expected dark counts measured.

Table 4.4: Overview of the datasets to obtain the dark current. Only exposure time (EXP), given in ms, was varied, and is denoted under settings.

Dataset (no.)	Date	HSI	Settings
DARK1	09.11.2018	HSI V6	EXP = 10
DARK2	09.11.2018	HSI V6	EXP = 15
DARK3	09.11.2018	HSI V6	EXP = 20
DARK4	09.11.2018	HSI V6	EXP = 25
DARK5	09.11.2018	HSI V6	EXP = 30
DARK6	09.11.2018	HSI V6	EXP = 35
DARK7	09.11.2018	HSI V6	EXP = 40

Table 4.5: Overview of the datasets for radiometric calibration. Frames per second (FPS) and exposure time (EXP), given in ms, was varied, and are denoted under settings.

Dataset (no.)	Date	HSI	Settings
RAD1	11.10.2018	HSI V4C	FPS=2, EXP=30
RAD2	11.10.2018	HSI V4C	FPS=2, EXP=30

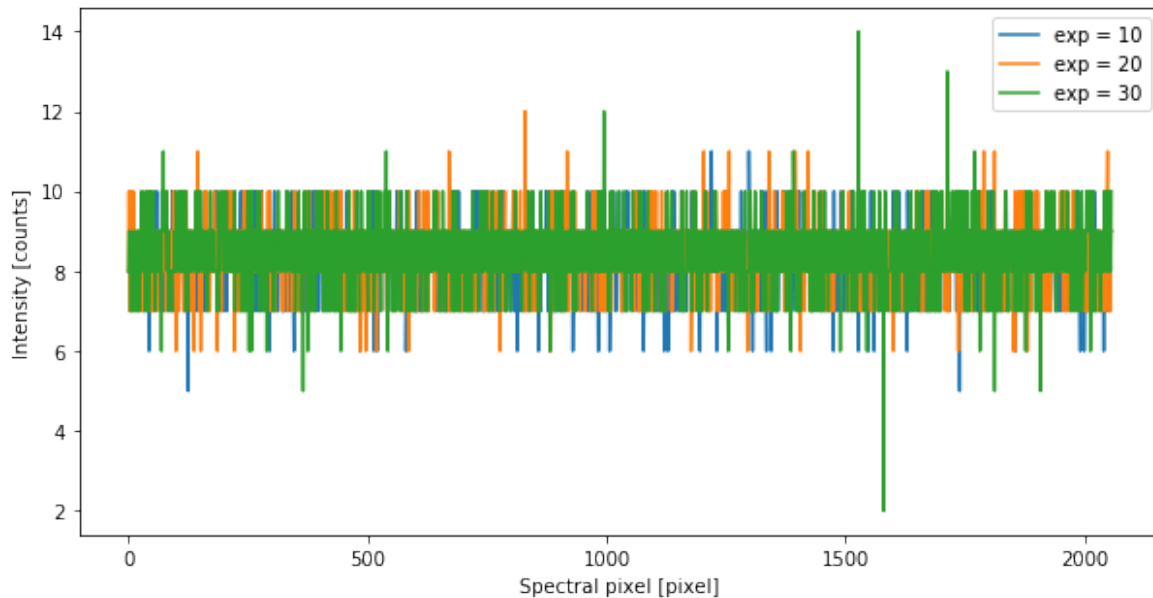
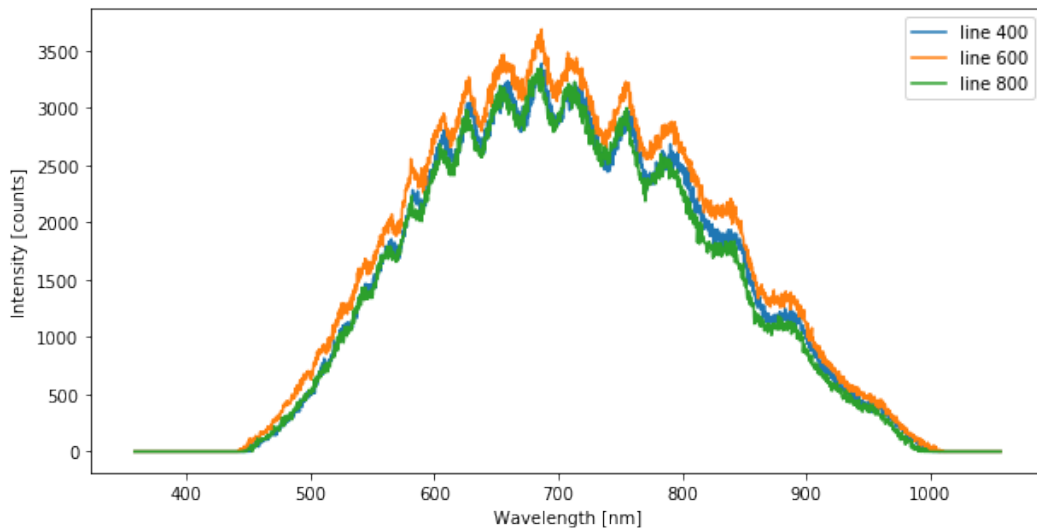


Figure 4.2: Dark current responses in line 500 in spectrograms from datasets DARK1, DARK3 and DARK5.

For the V6, the spectrogram consists of 1542 lines, lines around 600 are therefore close to the centre of the slit, while line 200 is closer to the edge of the image. In general, longer exposure time gives a more varied response. For further analysis, all pixels should be checked and compared. Several spectrograms within several datasets should be used, and provide result in form of a matrix with the estimated dark current for each pixel, with uncertainties. This would give  $b_{0,i,j}$ , where  $i$  and  $j$  represents the pixel position. If the values appears to be correlated within the rows, columns or the whole image, the result may be simplified by giving an estimate of the dark current per row, column or spectrogram, instead of a full matrix.

The results from the second part of the radiometric calibration of HSI V4C can be found in Figure 4.3. The calibration coefficients from the spectral calibration was applied to show the response depending on wavelength. The spectrogram for the HSI V4C consists of 1088 lines, so line 600 which shows the strongest response is located approximately in the middle of the spectrogram.



*Figure 4.3: Radiometric response at line 400, 600 and 800 in spectrogram from dataset RAD1. Spectral calibration coefficients have been applied.*

Figure 4.3 shows that there is little to no response for wavelengths below 450 nm and above 1000 nm. The reference spectrum from the light source can be seen in Figure 4.4, and shows that the light source emits light both from below 450 nm and above 1000 nm. The full lamp specifications can be found in Appendix A. The upper limit of the measured response could be due to the low quantum efficiency for wavelengths around or above 1000 nm in the imaging sensor, as seen in Figure 4.5.

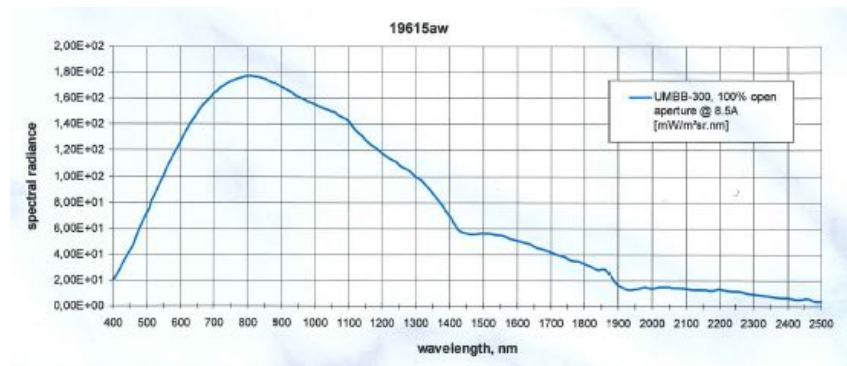


Figure 4.4: Radiometric lamp response, from lamp certificate in Appendix A.

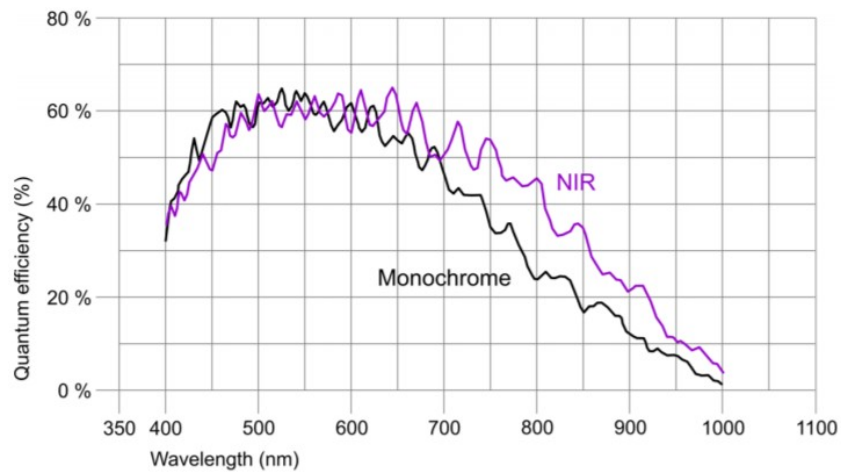


Figure 4.5: Quantum efficiency as a function of wavelength for the uEye UI-3360CP-NIR-GL camera head that is used for the HSI V4C. Figure from [44].

The ripples seen in the measured response can also be recognised from the quantum efficiency plot. Another possible explanation for both the upper and lower limit of the measured spectrum could be the coating on the lenses used in the imaging system.

As seen in the figures, the measured spectra in Figure 4.3 does not match up with the reference spectrum in Figure 4.4, which is why the radiometric calibration is needed. To find the calibration coefficient  $K_{i,j}$  for each pixel  $(i, j)$ , the measured response should be compared to the expected response of the reference source, as described in Equation 2.2.

### 4.3 Characterisation

The results presented in this section are the preliminary results for the characterisation procedure, and consists mainly of the detection and correction of the smile effect in Section 4.3.1, and estimation of the spectral bandpass in Section 4.3.2.

Detection and correction of the keystone effect should also be included in the characterisation procedure in the future. A collimator set-up for keystone detection has been designed and built, as described in Section 3.1.2. The next step for detecting keystone is to use the collimator set-up together with a hyperspectral imager to obtain spectrograms containing the striped pattern. A mounting structure for the collimator set-up should be designed to make the data acquisition more straightforward. By looking at the position of the line pattern at different wavelengths, an estimate of the keystone effect can be obtained and a correction method be developed.

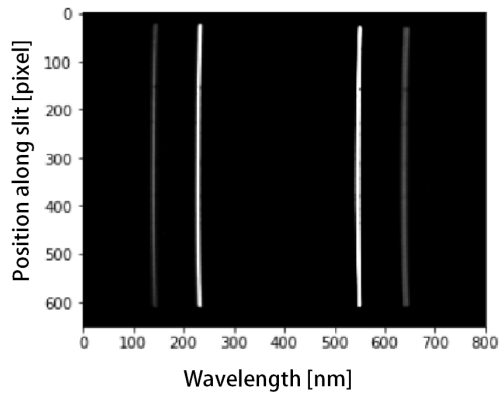
Further, it should be investigated whether the smile and keystone corrections can be corrected separately, or if they should be corrected simultaneously using the same dataset. To obtain data usable for detection of smile and keystone simultaneously, the collimator set-up can be used in combination with the spectral lamps that are used in the spectral calibration. The correction methods introduced in Section 2.3.3 should also be investigated further, and implemented if found suitable.

#### 4.3.1 Spectral Misregistrations (Smile)

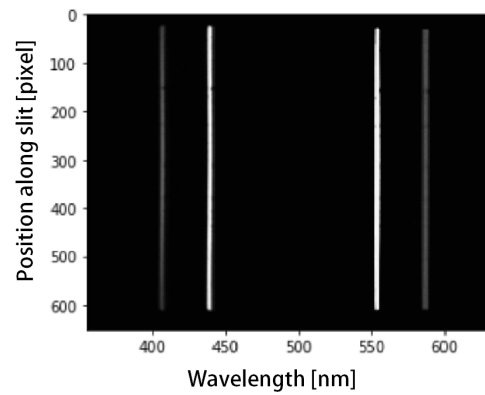
The smile effect was analysed using data from the HSI V4C. The same peaks from the mercury lamp in dataset SP3 and SP4, as used in the spectral calibration, were used. The detection and correction were made as described in Section 3.4.1, using a Python script developed by the NTNU SmallSat team. The results from the smile correction can be seen in Figure 4.6.

The smile effect causes the spectral lines in the spectrogram to appear bent, as seen in Figure 4.6a and 4.6c. When the smile correction is applied, the lines in the spectrogram should be straight, so that the pixels containing the peak of a spectral line are all in the same pixel column in the image.

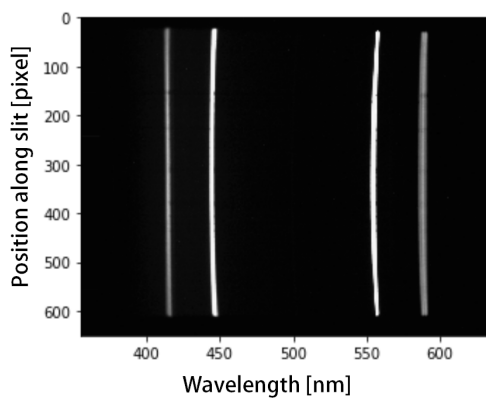
The smile correction works for dataset SP4, as seen in Figure 4.6b; the lines are straight after the image has been corrected. The correction of the spectrogram from dataset SP3, as seen



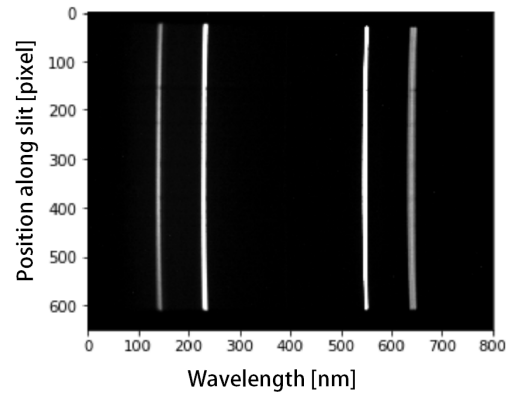
(a) Raw spectrogram, dataset SP4.



(b) Smile-corrected spectrogram, dataset SP4.



(c) Raw spectrogram, dataset SP3.



(d) Smile-corrected spectrogram, dataset SP3.

Figure 4.6: Effect of smile corrections. The spectrograms show peaks from the mercury lamp.

in Figure 4.6d, however, is not as good. The spectral lines are still bent after the correction has been made. This shows that the method used for detecting and correcting the smile effect needs more work, and should be improved.

A measurement of how bent or straight the lines are should be included in a future analysis. This will help quantifying the smile effect, both before and after correction has been made, and help make an estimate of how good the correction is. The metrics suggested in [26] should be considered when calculating the final value of both smile and keystone in the system.

### 4.3.2 Spectral bandpass

The spectral bandpass, FWHM, of the HSI V6 was estimated using the datasets SP9 and SP10 from the spectral calibration. The peaks used can be seen in Figure 4.7. An overview of the estimated bandpass of the different peaks can be seen in Table 4.6.

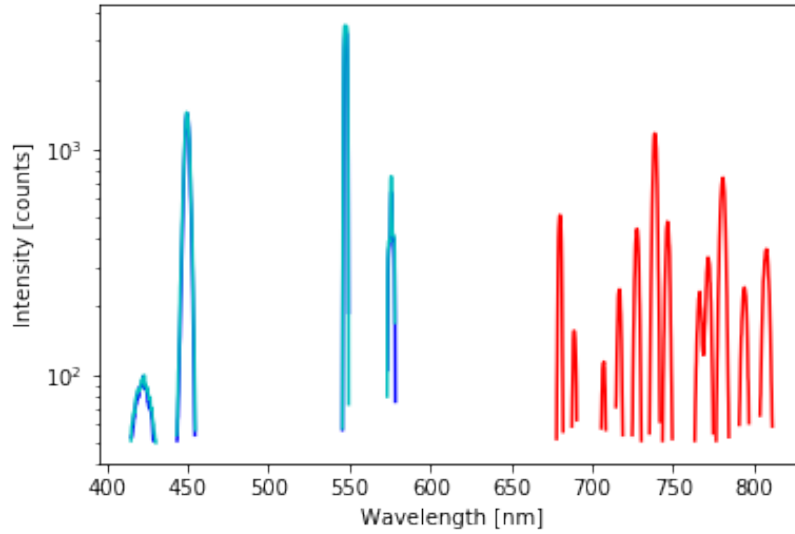


Figure 4.7: Peaks used for estimating the spectral bandpass. Red peaks are from the argon lamp, blue and cyan peaks from the mercury lamp at different slit heights. The peaks shown are only the ones above the threshold value.

The bandpass was found for one peak at the time, and the values then averaged to give an estimate of the spectral bandpass of the system. The maximum intensity of the peak was first detected, and half of this value used further as the half maximum value. The index of the max intensity peak was noted, and the index of the half maximum values on both sides found by iteratively moving away from the peak maximum, comparing the intensities to the half maximum value until finding a value below half maximum. The index, holding the pixel position, with the value closest to half maximum was chosen as the correct half maximum index. The difference between the wavelength values, given by the spectral calibration, belonging to each of these indices were then calculated, giving an estimation of the full width at half maximum. The average of all the estimated spectral bandpass values was found to be

$$FWHM \approx 3.85 \text{ nm.}$$

The expected spectral bandpass for the HSI V6 is approximately 3.3 nm, as seen in Section 3.1.1. The estimate found is therefore within the expectations.

*Table 4.6: Spectral bandpass estimated for the different peaks.*

Lamp	Peak no.	Line	FWHM	Lamp	Peak no.	Line	FWHM
Ar	1	462	2.87	Hg	2	462	4.30
Ar	3	462	3.28	Hg	3	462	2.66
Ar	4	462	3.69	Hg	4	462	4.10
Ar	5	462	3.48	Hg	1	616	4.51
Ar	6	462	3.69	Hg	2	616	2.87
Ar	7	462	4.3	Hg	3	616	3.89
Ar	8	462	4.51				
Ar	9	462	4.71				
Ar	10	462	4.92				

However, there are several improvements that can be done for the estimation of spectral bandpass. The calculation should be done for a greater number of lines, in order to cover differences in the bandpass with respect to slit height. When looking at the argon lines, the bandpass increases with peak number, which could indicate that the spectral bandpass depends on wavelength. This dependency should also be characterised. To find the wavelength value of the full width at half maximum, a better estimation can be done than just choosing the closest point. In addition, uncertainty estimates should also be added.



## 5 | Conclusion and Further Work

The aim of this project was to set up spectral and radiometric calibration procedures and investigate a method for detecting smile and keystone effects in hyperspectral imagers.

Spectral and radiometric calibration procedures were set up, and data obtained using two hyperspectral imagers. The results of both calibrations show that several images from datasets obtained with different settings should be used to give an estimated relationship between pixel and wavelength in spectral calibration, and sensor count and radiance in radiometric calibration. The data from spectral calibration was further used to detect and correct the smile effect, and to estimate the spectral bandpass of the system. In addition, a set-up to detect the keystone effect was proposed and built.

Future work includes acquiring more data for radiometric calibration using the same imager, so that an estimate of both the dark current and the radiometric response can be found for the imager, and give full radiometric calibration. The radiometric calibration analysis should then be finalised. Further, all of the data analysis should be expanded to include data from several spectrograms within several datasets collected with different camera settings. The results should then be averaged, and the uncertainties estimated. The final result of the calibrations should be a matrix the size of a frame, or smaller if the results are correlated. The collimator set-up designed for keystone detection should be tested with hyperspectral imagers before use. If the set-up works, data should be obtained and analysed to detect keystone in the system. Further, an algorithm for correcting keystone should be developed.

The data from radiometric calibration can further be used to find the SNR, dynamic range, and the linearity of the sensor. A set-up for detecting the PSF can also be developed for a more thorough characterisation of the system, as done in [25]. Other effects, such as temperature dependency, stray light, and polarisation sensitivity, as mentioned in [10], should also be characterised. In addition, since the hyperspectral imagers used in this report will be used in remote sensing, procedures and methods for performing calibration and corrections in-flight and in-orbit should also be developed.



# Bibliography

- [1] M. T. Eismann, *Hyperspectral Remote Sensing*. SPIE, 2012.
- [2] K. Lenhard, *Improving the Calibration of Airborne Hyperspectral Sensors for Earth Observation*. PhD thesis, University of Zurich, 2015.
- [3] P. M. Gilbert, D. M. Anderson, P. Gentien, E. Granéli, and K. G. Sellner, “The Global Complex Phenomena of Harmful Algal Blooms,” *Oceanography*, vol. 18, no. 2, pp. 136–147, 2005.
- [4] J. H. Landsberg, “The effects of harmful algal blooms on aquatic organisms,” *Reviews in Fisheries Science*, vol. 10, no. 2, pp. 113–390, 2002.
- [5] M. E. Grøtte *et al.*, “Hyperspectral Imaging Small Satellite in Multi-Agent Marine Observation System,” 2018.
- [6] K. Rajan, T. A. Johansen, and R. Birkeland, “A Roadmap for a SmallSat Program,” 2016.
- [7] J. S. Pearlman, P. S. Barry, C. C. Segal, J. Shepanski, D. Beiso, and S. L. Carman, “Hyperion, a space-based imaging spectrometer,” *IEEE Transactions on Geoscience and Remote Sensing*, vol. 41, no. 6, pp. 1160–1173, 2003.
- [8] R. L. Lucke *et al.*, “The hyperspectral imager for the coastal ocean (hico) - design and early results,” *IGRSS Workshop on Hyperspectral Image and Signal Processing: Evolution in Remote Sensing*, 2010.
- [9] J. Transon, R. d’Andrimont, A. Maignard, and P. Defourny, “Survey of Hyperspectral Earth Observation Applications from Space in the Sentinel-2 Context,” *Remote Sensing*, vol. 10, no. 157, pp. 1–32, 2018.
- [10] C. McClain and G. Meister, *Mission Requirements for Future Ocean-Colour Sensors*, vol. 13. IOCCG, 2012.
- [11] P. Gege *et al.*, “Calibration facility for airborne imaging spectrometers,” *ISPRS Journal of Photogrammetry and Remote Sensing*, vol. 64, no. 4, pp. 387–397, 2009.
- [12] X. Yu, Y. Sun, A. Fang, W. Qi, and C. Liu, “Laboratory spectral calibration and radiometric calibration of hyper-spectral imaging spectrometer,” *2nd International Conference on Systems and Informatics*, pp. 871–875, 2014.
- [13] T. Skauli, H. E. Torkildsen, S. Nicolas, T. Opsahl, T. Haavardsholm, I. Kåsen, and A. Rognmo, “Compact camera for multispectral and conventional imaging based on patterned filters,” *Applied Optics*, vol. 53, no. 13, 2014.
- [14] F. Sigernes, *Basic Hyper Spectral Imaging*. 2018.
- [15] G. Joseph, *Building Earth Observation Cameras*. Taylor & Francis Group, 2015.
- [16] Y. Zong, S. W. Brown, G. Meister, R. A. Barnes, and K. R. Lykke, “Characterization and correction of stray light in optical instruments,” *SPIE*, vol. 6744, 2007.
- [17] G. Yang, C. Li, Y. Wang, H. Yuan, H. Feng, B. Xu, and X. Yang, “The DOM generation and precise radiometric calibration of a UAV-mounted miniature snapshot hyperspectral imager,” *Remote Sensing*, vol. 9, no. 642, 2017.
- [18] P. Mouroulis, R. O. Green, and T. G. Chrien, “Design of pushbroom imaging spectrometers for optimum recovery of spectroscopic and spatial information,” *Applied Optics*, vol. 39, no. 13, 2000.
- [19] J. J. Sellers, *Understanding Space, An Introduction to Astronautics*. McGraw-Hill Custom Publishing, 2004.
- [20] F. Sigernes *et al.*, “Sensitivity calibration of narrow field of view optical instruments,”

- [21] D. Tao, G. Jia, Y. Yuan, and H. Zhao, "A digital sensor simulator of the pushbroom offner hyperspectral imaging spectrometer," *Sensors (Basel, Switzerland)*, vol. 14, pp. 23822–23842, 2014.
- [22] N. Yokoya, N. Miyamura, and A. Iwasaki, "Detection and correction of spectral and spatial misregistrations for hyperspectral data using phase correlation method," *Applied Optics*, vol. 49, no. 24, pp. 4568–4575, 2010.
- [23] N. Yokoya, N. Miyamura, and A. Iwasaki, "Preprocessing of hyperspectral imagery with consideration of smile and keystone properties," *Proc. SPIE 7857, Multispectral, Hyperspectral, and Ultraspectral Remote Sensing Technology, Techniques, and Applications III, 78570B*, 2010.
- [24] A. Fridman, G. Høye, and T. Løke, "Resampling in hyperspectral cameras as an alternative to correcting keystone in hardware, with focus on benefits for optical design and data quality," *Optical Engineering*, vol. 53, no. 5, 2014.
- [25] T. Skauli and H. E. Torkildsen, "Measurement of point spread function for characterization of coregistration and resolution: comparison of two commercial hyperspectral cameras," *Algorithms and Technologies for Multispectral, Hyperspectral, and Ultraspectral Imagery XXIV*, 2018.
- [26] T. Skauli, "An upper-bound metric for characterizing spectral and spatial coregistration errors in spectral imaging," *Optics Express*, vol. 20, no. 2, 2012.
- [27] H. E. Torkildsen and T. Skauli, "Full characterization of spatial coregistration errors and spatial resolution in spectral imagers," *Optics Letters*, vol. 43, no. 16, pp. 3814–3817, 2018.
- [28] R. Horaud, R. Mohr, and B. Lorecki, "On single-scanline camera calibration," *IEEE Transactions on Robotics and Automation*, vol. 1, no. 9, pp. 71–75, 1993.
- [29] C. A. Luna, M. Mazo, J. L. Lazaro, and J. F. Cazquez, "Calibration of Line-Scan Cameras," *IEEE Transactions on instrumentation and measurement*, vol. 59, no. 8, pp. 2185–2190, 2010.
- [30] V. Miljković, D. Gajski, and E. Vela-Zagreb, "Spatial calibration of the hyperspectral line scanner by the bundle block adjusting method," *Geodetski List*, vol. 71, no. 2, pp. 127–142, 2017.
- [31] D. Li, G. Wen, B. Wei Hui, S. Qiu, and W. Wang, "Cross-ratio invariant based line scan camera geometric calibration with static linear data," *Optics and Lasers in Engineering*, vol. 62, pp. 119–125, 2014.
- [32] D. Su, A. Bender, and S. Sukkarieh, "Improved cross-ratio invariant-based intrinsic calibration of a hyperspectral line-scan camera," *Sensors*, vol. 18, 2018.
- [33] D. Z. für Luft-und Raumfahrt e.V., "The calibration home base for imaging spectrometers," *Journal of large-scale research facilities*, vol. 2, no. A82, 2016.
- [34] K. C. Lawrence, B. Park, W. R. Windham, and C. Mao, "Calibration of a pushbroom hyperspectral imaging system for agricultural inspection," *American Society of Agricultural Engineers*, vol. 46, no. 2, pp. 513–521, 2003.
- [35] Oriel Instruments, "Typical Spectra of Oriel Instruments Spectral Calibration Lamps." [https://www.newport.com/medias/sys\\_master/images/images/h55/hfd/8797293281310/Typical-Spectra-of-Spectral-Calib-Lamps.pdf](https://www.newport.com/medias/sys_master/images/images/h55/hfd/8797293281310/Typical-Spectra-of-Spectral-Calib-Lamps.pdf). (online) [Accessed: November 6, 2018].
- [36] F. Sigernes *et al.*, "Do it yourself hyperspectral imager for handheld to airborne operations," *Optics Express*, vol. 26, no. 5, pp. 6021–6035, 2018.
- [37] F. Sigernes *et al.*, "Pushbroom Hyper Spectral Imager version 6 (HSI v6) part list – Final prototype," 2018.
- [38] Gigahertz-Optik, "ISS-30-VA." <https://www.gigahertz-optik.de/en-us/product/ISS-30-VA>. (online) [Accessed: November 6, 2018].
- [39] Newport, "Spectral Calibration Lamp, Argon, 10 mA, 500 Hrs Rated Life, Model: 6030." <https://www.newport.com/p/6030>. (online) [Accessed: November 6, 2018].

- [40] Newport, "Spectral Calibration Lamp, Krypton,  $10 \pm 4$  mA, 1000 Hrs Rated Life, Model: 6031." <https://www.newport.com/p/6031>. (online) [Accessed: November 6, 2018].
- [41] Newport, "Spectral Calibration Lamp, Xenon,  $6 \pm 3$  mA, 250 Hrs Rated Life, Model: 6033." <https://www.newport.com/p/6033>. (online) [Accessed: November 6, 2018].
- [42] Newport, "Spectral Calibration Lamp, Hg (Ar),  $18 \pm 5$  mA, 5000 Hrs Rated Life, Model: 6035." <https://www.newport.com/p/6035>. (online) [Accessed: November 6, 2018].
- [43] Newport, "Lamp Power Supply, AC, Xenon, 6 mA, 220 VAC, 50 Hz." <https://www.newport.com/p/6044>. (online) [Accessed: December 7, 2018].
- [44] IDS, "UI-3360CP-NIR-GL Rev.2 (AB00624)." [https://en.ids-imaging.com/IDS/datasheet\\_pdf.php?sku=AB00624](https://en.ids-imaging.com/IDS/datasheet_pdf.php?sku=AB00624). (online) [Accessed: December 16, 2018].
- [45] Gigahertz-Optik GmbH, "Calibration certificate," 2013.



# Appendices



# A | Lamp Certificate, ISS-30-VA

The calibration lamp certificate belonging to the integrating sphere used in the calibrations can be seen in Figure A.1 to A.4.

Kalibrierlaboratorium für optische Strahlungsmessgrößen  
*Calibration laboratory for optical radiometry*



## GIGAHERTZ OPTIK GMBH

**Werkskalibrierschein**  
**Calibration Certificate**

Kalibrierzeichen  
 Calibration mark

19615
WERK
2013-02

Gegenstand <i>Object</i>	<b>Homogene Lichtquelle für spektrale Strahl-dichte</b> <b>Homogeneous light source for spectral radiance</b>
Hersteller <i>Manufacturer</i>	<b>Gigahertz-Optik, GmbH</b>
Typ <i>Type</i>	<b>UMBB-300 / LPS-100-RM / X1-RM / LS-OK-30-VA / VL-1101-4</b>
Fabrikate/Serien-Nr. <i>Serial number</i>	<b>19615aw / 13364M / 12668M / 23031</b>
Auftraggeber <i>Customer</i>	<b>Norsk Elektro Optikk A/S</b> <b>Solheimveien 62A</b> <b>N-1473 Lorenskog NORWAY</b>
Auftragsnummer <i>Order No.</i>	<b>PO 1012241 / (19615)</b>
Anzahl der Seiten des Kalibrierscheines <i>Number of pages of the certificate</i>	<b>5</b>
Datum der Kalibrierung <i>Date of calibration</i>	<b>15. February 2013</b>

Dieser Kalibrierschein dokumentiert die Rückführung auf nationale Normale zur Darstellung der Einheiten in Übereinstimmung mit dem Internationalen Einheitensystem (SI).

Das Kalibrierlaboratorium arbeitet in Anlehnung an die DIN EN ISO/IEC 17025. Die internen Transfernormale werden regelmäßig gegen Normale kalibriert, welche einen DKD-Kalibrierschein haben oder rückführbar auf ein Normal mit DKD-Kalibrierschein kalibriert sind oder gegen Normale eines nationalen Metrologieinstituts kalibriert sind.

Für die Einhaltung einer angemessenen Frist zur Wiederholung der Kalibrierung ist der Benutzer verantwortlich.

*This calibration certificate documents the traceability to national standards, which realise the units of measurement according to the International System of Units (SI).*

*The calibration laboratory works based to the DIN EN ISO/IEC 17025. The intern used transfer standards were regular calibrated against standards, which have DKD certificates or are traceable to a standard with DKD or National Metrology Institute certificate.*

*The user is obliged to have the object recalibrated at appropriate intervals.*

Dieser Kalibrierschein darf nur vollständig und unverändert weiterverbreitet werden. Auszüge oder Änderungen bedürfen der Genehmigung des ausstellenden Kalibrierlaboratoriums. Kalibrierscheine ohne Unterschrift und Stempel haben keine Gültigkeit.

*This calibration certificate may not be reproduced other than in full except with the permission the issuing laboratory.*

*Calibration certificates without signature and seal are not valid.*



Datum  
Date

15. February 2013

Leiter des Kalibrierlaboratoriums  
Head of the calibration laboratory

Dipl.-Ing. (FH) Anton Gugg-Helminger

Mitarbeiter im Kalibrierlabor  
Person of Charge

Dipl.-Ing. (FH) Richard Rendle

Figure A.1: Lamp certificate, page 1 [45].



19615

WERK

2013-02

Seite 2 zum Kalibrierschein vom 15. February 2013  
Page of calibration certificate dated

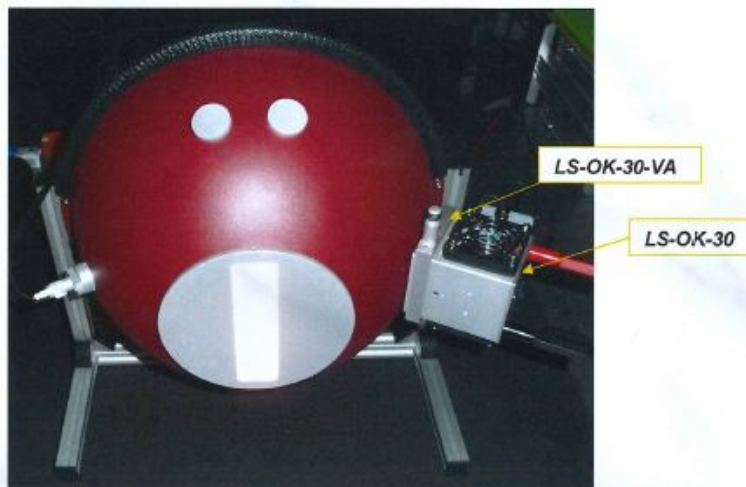
### 1. Description of the calibration object:

The calibration object is an integrating sphere, type UMBB-300 / LPS-100-RM / X1-RM / LS-OK-30-VA / VL-1101-4, SN 19615aw / 13364M / 12668M / 23031, inside made from BaSO<sub>4</sub>. The sphere is fixed inside a stable aluminium frame.

On one side of the sphere is a lamp housing with a light source, type LS-OK-30 mounted with diffuse transmitting baffle. The lamp SN L1837 is a frosted 100W QH lamp, (unfrosted type: Osram 12V, 100W, HLX 64623). On the housing frame are two cooling fan's. In front of the light source is a manually adjustable variable attenuator, LS-OK-30-VA mounted.

To connect the light source to the power supplies LPS-100-RM use the red and black cable.

On the sphere there is a photometric detector head, VL-1101-4 which is read out by the Optometer X1-RM.



Picture 1: measurement object

### 2. Measurement:

The spectral radiance was measured by using a calibration reference source, type SRS8Q, SN 7421 (Last Calibration in May 2012; GO327-WERK-2012-05), that is traceable to the PTB (Physikalisch Technischen Bundesanstalt). A monochromator (TM300) was horizontal to his input optic (telescope) measured by the calibration object and by the reference. The irradiation was measured with a silicon and a PbS detector.

### 3. Conditions during the measurement:

The calibration object and the reference were measured in rapid succession horizontal to the telescope. The measured optical surface was focused by the telescope. The measuring field of view was by  $\varnothing 7\text{mm}$ . The calibration object was calibrated by all lamps together and for the variable attenuator at 100 % intensity.

#### **Spectral bandwidth of the monochromator**

Full width half measured (FWHM)

FWHM = 10 nm for  $400\text{ nm} \leq \text{Lambda} \leq 1100\text{ nm}$

FWHM = 20 nm for  $1100\text{ nm} < \text{Lambda} \leq 2500\text{ nm}$



19615

WERK

2013-02

Seite 3 zum Kalibrierschein vom 15. February 2013  
 Page of calibration certificate dated

**Current of the lamp:**

The Reference SRS8Q, SN 7421 was operated by a dc stabilised power supply Gigahertz-Optik type LPS250, SN 3623M at a current of 4.000A.

The calibration object UMBB-300 / LPS-100-RM / X1-RM / LS-OK-30-VA / VL-1101-4, SN 19615aw / 13364M / 12668M / 23031 was operated by using the internal power supplies LPS-100-RM of the corresponding electronic Device.

The internal current **setting of the power supplies LPS-100-RM are 8.5A.**

The calibration standard was set on at least 30 minutes before measurement.

**Temperature:**

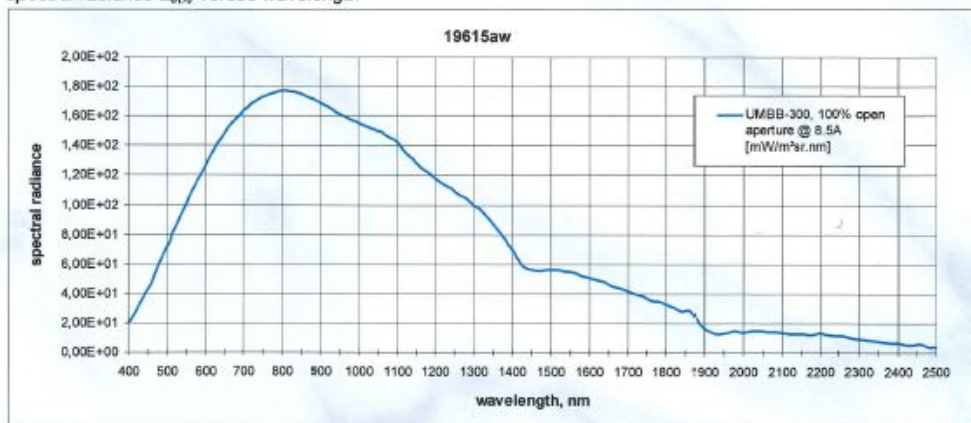
Between 24 °C +/- 3 °C

**Burning time:**

2 h within the time of calibration

**4. Result of the measurement:**

Spectral radiance  $L_{e,\lambda}$  versus wavelength



Numerical value

The numerical values are on Data-CD 19615aw-k.xls

Figure A.3: Lamp certificate, page 3 [45].



19615

WERK

2013-02

Seite 4 zum Kalibrierschein vom 15. February 2013  
 Page of calibration certificate dated

Calculated values	19615aw UMBB-300, 100% open aperture
For lamp current	8.50 A
Integrated radiance	42.95 W/(sr m <sup>2</sup> )
Luminance	7612 cd/m <sup>2</sup>
Color coordinates	x = 0.4240
	y = 0.4028
Correlated color temperature	3217 K
Measuring range	380nm - 780nm

Into the X1-RM is the following value as calibration factor stored:

Kalibrierfaktor Calibration factor	0.200nA/(cd/m <sup>2</sup> )
---------------------------------------	------------------------------

For the relative spectral uncertainty is following table responsible:

Wavelength [nm]	Relative uncertainty [%]
400nm up to 420nm in 10nm steps	± 6
430nm up to 1100nm in 10nm steps	± 4
1120nm up to 1500nm in 20nm steps	± 7.5
1520nm up to 2300nm in 20nm steps	± 9
2320nm up to 2350nm in 20nm steps	± 12
2370nm up to 2400nm in 20nm steps	± 14
2420nm up to 2500nm in 20nm steps	± 15

The uncertainty for the correlated colour temperature = +/- 50K.  
 The uncertainty for the luminance meter = +/- 3%.

##### 5. Remarks:

The calibration number 19615 - WERK - 2013-02 is marked on the calibration unit Type UMBB-300 / LPS-100-RM / X1-RM / LS-OK-30-VA / VL-1101-4, SN 19615aw / 13364M / 12668M / 23031. The calibration is only valid with the listed power supply. The calibration values are stored on CD.

A dependence of the spectral radiance from other as the given conditions is not examined. It is reckon in a wavelength dependence spectral radiance during the life of the lamp and a change in correlated colour temperature.

A regular recalibration of the calibrated unit type UMBB-300 / LPS-100-RM / X1-RM / LS-OK-30-VA / VL-1101-4, SN 19615aw / 13364M / 12668M / 23031 is recommended.

Figure A.4: Lamp certificate, page 4 [45].